Theoretical and Applied Climatology (2024) 155:3329–3346
https://doi.org/10.1007/s00704-023-04804-7

RESEARCH

Subsea permafrost and associated methane hydrate stability zone: how long can they survive in the future?

Valentina V. Malakhova[1] · **Alexey V. Eliseev**[2,3,4]

Received: 16 March 2023 / Accepted: 12 December 2023 / Published online: 4 January 2024

Abstract

The simulations with SMILES (the Sediment Model Invented for Long-tErm Simulations) for 100 kyr in the future driven by the output of an Earth System Model with internally calculated ice sheets are performed. This Earth System Model was forced by idealised scenarios of CO_2 emissions and by changes of the parameters of the Earth's orbit. The simulations are carried out with different values of the heat flux from the Earth's interior. We neglected the possible impact of hydrostatic pressure changes due to future sea level changes on freeze/thaw temperature and on thermodynamic stability of methane hydrates. We found that at the outer shelf, permafrost disappears either before the onset of the anthropogenic emissions or during a few centuries after it. In contrast, for the middle and shallow parts of the shelf, in the CO_2-emission forced runs, the subsea permafrost survives, at least, for 5 kyr after the emission onset or even for much longer. At the same parts of the shelf, methane hydrate stability zone (MHSZ) disappears not earlier than at 3 kyr after the CO_2 emission onset. Both permafrost thaw and methane hydrate stability zone shrinking occur mostly from the bottom and depend strongly on the heat flux from the Earth's interior. However, permafrost thaw from the top is basically determined by the applied CO_2 forcing scenario. In general, the CO_2-induced warming in our simulations is able to enhance the pan-Arctic subsea permafrost loss severalfold during 1 kyr after the emissions onset, but it is less important for the respective MHSZ loss. The dynamics of MHSZ is largely independent on the chosen climate projection, at least for the next several thousand years.

1 Introduction

The methane hydrates at the contemporary Arctic shelf are believed to develop during the glaciations of the Pleistocene, when the sea level was substantially lower than the present-day one, and this shelf was in a direct contact with a cold atmosphere (MacDonald 1990; Buffett 2000; Romanovskii et al. 2005; O'Connor et al. 2010; Shakhova et al. 2019; Gavrilov et al. 2020b; Bogoyavlensky et al. 2023. This contact allowed for permafrost development in the exposed shelf (Romanovskii et al. 2005; Portnov et al. 2014; Majorowicz et al. 2012; Overduin et al. 2019; Angelopoulos et al. 2020), thus providing necessary conditions for the thermodynamic stability of methane hydrates within the methane hydrate stability zone (MHSZ)—the volume of the sediments where the thermophysical state of the subsea sediments is favourable for hydrate formation. Both the subsea permafrost and the permafrost-associated methane hydrates (PAMH) are known to exist at the present day, possibly owing to their long, of the order of 10^1 kyr (Romanovskii et al. 2005; Mestdagh et al. 2017; Malakhova and Eliseev 2017, 2020b), response time scales to temperature anomaly at the top of the sediments. An observational support for the existence of both the subsea permafrost and the permafrost-associated methane hydrates is available from the data which employs either seismic (Bogoyavlensky et al. 2022, 2023) or electromagnetic (Koshurnikov 2023; Alekseev et al. 2023) measurements in the sediments.

A natural question arises on how long the subsea permafrost and PAMH would not disappear given the ongoing

✉ Valentina V. Malakhova
malax@sscc.ru

Alexey V. Eliseev
eliseev.alexey.v@mail.ru

[1] Institute of Computational Mathematics and Mathematical Geophysics, Siberian Branch of the Russian Academy of Sciences, 6 Acad. Lavrentyev Av., Novosibirsk 630090, Russia

[2] Physical Faculty, Lomonosov Moscow State University, 1 Vorobyevy Gory, Moscow 119991, Russia

[3] A.M. Obukhov Institute of Atmospheric Physics, 3 Pyzhevsky, Moscow 119017, Russia

[4] Institute of Environmental Sciences, Kazan Federal University, 5 Tovarishcheskaya, Kazan 420097, Russia

climate warming and future changes in the parameters of the Earth's orbit. While temperature changes at the sea floor at the shelf are projected to be rather modest at the century timescale even under relatively strong anthropogenic warming (Lamarque 2008; Heuzé et al. 2015; Bogoyavlensky et al. 2018; Chuvilin et al. 2022), a stronger warming may occur at a larger time scale. One possible mechanism for this is due to the riverine export of sensible heat (Dmitrenko et al. 2011; Yang et al. 2014; Golubeva et al. 2018; Shakhova et al. 2019). An additional mechanism is a formation of a deep mixing layer in summer in ice-free regions (Lique et al. 2018). Such regions may become widespread because the contemporary warming will proceed further (Notz 2020). In turn, a deep mixing layer may efficiently transport heat from the oceanic surface down to the floor, which is exhibited both in the observational studies in the Barents Sea (Ivanov 2023) and in future projections with detailed climate models over the whole Arctic shelf (Lique et al. 2018; Malakhova and Eliseev 2023).

As a result, at millennium and longer timescales, the thermal state of the subsea sediments may be changed markedly with respective impacts on the subsea permafrost and PAMH MHSZ. For instance, Wilkenskjeld et al. (2021) projected an accelerated degradation of the subsea permafrost during the next millennium. This is in a stark contrast with the results by Matveeva et al. (2020), who projected that the subsea permafrost exists and the PAMH are thermodynamically stable for, at least, several kiloyears after the present assuming that there is no anthropogenic climate forcing in the atmosphere Further, in simulations by Hunter et al. (2013) until 2850 C.E. (common era), methane release from the hydrate dissociation either accelerates during the incoming millennium or exhibits a peak followed by a decline depending on the applied warming scenario. Even longer, 20 kyr and 100 kyr-scale, future projections were performed, correspondingly by Majorowicz et al. (2012) and by Archer (2015).

All these projections except that by Majorowicz et al. (2012) neglect future changes in parameters of the Earth's orbit, thus a possible next glacial inception. It was simulated earlier that both the subsea permafrost and PAMH MHSZ were markedly thinner or even non-existent at the middle and outer parts of the Arctic shelf following the Pleistocene glacial terminations (Romanovskii et al. 2005, 2006; Majorowicz et al. 2012; Malakhova and Eliseev 2017, 2018, 2020b, a; Gavrilov et al. 2020a). Next glacial inception, in turn, may be delayed because of the ongoing, mostly CO_2-induced climate warming (Archer and Ganopolski 2005; Ganopolski et al. 2016). Thus, it is of considerable interest to study the impact of these two forcings combined.

A related problem is due to the measurable present-day dissociation of hydrates with the gas venting out from the sediments to the water and further from the water to the atmosphere (Buffett 2000; Romanovskii et al. 2005; O'Connor et al. 2010; Shakhova et al. 2010; Anisimov et al. 2012; Majorowicz et al. 2015; Chuvilin et al. 2018; Shakhova et al. 2019). Methane hydrate dissociation was also inferred from the isotope measurements as a possible cause for the development of past hot epochs (e.g., the Paleocene-Eocene Thermal Maximum, Dickens et al. 1995; Zeebe 2012). Large spatial and seasonal variability associated with these emissions hamper even the present-day pan-Arctic estimates of this source. In particular, while most studies, including the Intergovernmental Panel On Climate Change Working Group 1 Sixth Assessment Report (IPCC WG1 AR6), conclude that total methane flux from the surface of all (including both the Arctic Ocean and other oceans) shelf areas to the atmosphere is $\leq 10\,\mathrm{TgCH_4\,yr^{-1}}$ (Saunois et al. 2020; Canadell et al. 2021), there are claims that this flux may be markedly larger (e.g., Shakhova et al. 2010).

These fluxes might become much stronger when permafrost and hydrate layers completely disappeared, especially given the upper estimate of the methane stock in the submerged permafrost-associated hydrates of 1400 PgC (Shakhova et al. 2010; James et al. 2016). A necessary ingredient for such enhancement is an accumulation within and below the frozen sediment layer of the methane from the hydrates dissolved in the lower part of MHSZ (Majorowicz et al. 2012; Sapart et al. 2017). This trapped gas stays below the shrinking MHSZ until the impermeable layer disappears, and a pulse release of methane might occur afterwards. Despite such a catastrophic release may be attenuated by the transient existence of pathways through taliks that form below paleo-river channels, lakes, and lagoons, especially in regions with high geothermal heat flux (Frederick and Buffett 2014; Majorowicz et al. 2015; Malakhova and Eliseev 2018; Angelopoulos et al. 2021), any information on the timing of such potentially catastrophic release is of prominent interest.

This goal is pursued in the present paper. We employ idealised simulations with a model for sediment thermophysics forced by the most relevant climate forcings: slow variations due to the evolution of the Earth's orbit and due to a century-scale anthropogenic greenhouse warming followed by a relaxation of the atmospheric CO_2 content because of its uptake by the ocean and by the terrestrial ecosystems.

For methane hydrates, we limit our study only for their stability zone. Thus, hydrates may or may not be present within this volume depending on the local availability of methane. Moreover, even when MHSZ disappears within a given volume of the subsea sediments, methane hydrates might be present here for several centuries because of energy constraints and because of the self-conservation phenomenon (Ruppel and Kessler 2017; Chuvilin et al. 2018).

Our simulation setup lacks an explicit geography but observes the dependence of the climate forcing in the Pleistocene on the contemporary shelf depth. The latter dependence is reflected in lengths of time intervals when shelf is either inundated or exposed to the atmosphere—this is an essential ingredient for resolving the dynamics of the thermodynamical properties in the different parts of the Arctic shelf at different timescales.

2 Model and simulations

We use the version of the SMILES (the Sediment Model Invented for Long-tErm Simulations) which is identical to that described in Malakhova and Eliseev (2020a). It has evolved from the model for sediment thermophysics (Denisov et al. 2011; Eliseev et al. 2015; Malakhova and Golubeva 2016; Malakhova and Eliseev 2017, 2018, 2020b) by extending the earlier model version with an equation for salt diffusion in the sediment pores. In brief, the model solves two coupled one-dimensional diffusion equations: one is for heat diffusion in the sediments (taking into account heat which is consumed during thaw or released during freezing), and another one is for salt diffusion in the sediments. Both equations are solved in the sediment column of depth $H_S = 1500$ m. For heat diffusion equation, a Stefan condition is imposed at the thaw/freezing interfaces in the sediments. For the same equation, heat capacity and thermal conductivity depend on the state of the sediment layer (either frozen or unfrozen; Table S1). Salt diffusion is allowed in the unfrozen layers only. Freeze/thaw temperature depends on salinity and pressure, thus leading to the coupling between heat and salt diffusion equations. The latent heat of fusion during the formation and melting of the pore ice is explicitly accounted for, but the respective heat released during the dissociation of hydrates is neglected. Sediment porosity ϕ exponentially decreases downward from the value of 0.4 at the top of the sediments with the vertical scale of 2500 m. Heat and salt diffusion equations are solved at a vertical grid with a step of 0.5 m. Lithological stratification in the vertical is figured in Table S1. This setup corresponds to the sediment drilling measurements in the Laptev Sea Razumov et al. (2014); Gavrilov et al. (2020a).

Equilibrium methane hydrate stability boundary is adapted from the TOUGH+HYDRATE model taking into account salt-induced depression of the dissociation temperature (Reagan and Moridis 2008; Reagan et al. 2011.

The complexity of our model is comparable to the model employed by Matveeva et al. (2020) except they neglect salinity variations while we neglect the latent heat of methane hydrate dissociation. Another example is the model used by Archer (2015), which thermophysical module is similar to ours, but neglects the salinity diffusion in the sediment pores. Our model was verified against the drilling measurements at the New Siberian Islands (Gavrilov et al. 2020a) as well as against the onshore measurements (Arzhanov and Malakhova 2023). A more detailed description of SMILES is available in the supplement (Section S1).

The simulations are performed for three values of the present-day shelf depth H_B: 10 m, 50 m, and 100 m. These ‘locations’ do not represent any particular geographic points, Rather, they are assumed to be representative for the shallow, intermediate (or middle), and deep (or outer) parts of the shelf correspondingly. We highlight that here and below the term ‘the present-day shelf depth’ means the thickness of water layer above the sea floor at the present day.

Initial conditions for both heat and salt diffusion equations are applied for a non-glacial state as it is reconstructed for 400 kyr B.P. (before present). Here, ‘present’ (or time instant $t = 0$) is formally ascribed to year 1950 C.E.

At the sediment–ocean interface (or at the sediment–air interface if the sediments are in contact with the air during marine regressions), temperature and salinity are prescribed to time-dependent functions T_B and S_B.

When shelf is in contact with the atmosphere, T_B is set equal to surface air temperature (SAT) T_a, and S_B is zeroed. When shelf is covered by water, T_B (S_B) is prescribed to be equal to the near-bottom water temperature (salinity) T_w (S_w). For past time instants and for the present day ($t \leq 0$), both T_w and S_w depend only on the present-day shelf depth H_B (Table S3). At the bottom of sediment domain, time-independent heat flux G from the Earth’s interior and no-flux condition for salinity are adapted. The time-dependent T_a is constructed from the monthly mean SAT simulated with the Climber-2 for time interval from 400 kyr B.P. to $t = 0$ (Ganopolski et al. 2016) as it is detailed in supplementary Section S3. The temperature and salinity profiles as simulated for $t = 0$ are shown in supplementary Fig. S5.

Then, our simulations are continued for another 100 kyr. We loosely refer to this time interval as a ‘future’ ($t > 0$) and mark it with ‘after present’ (A.P.). In this, we assume that the shelf is always covered by water, but SAT changes. Thus, for future $T_B = T_w + \Delta T_{fut}$ (Fig. S2). In the first series of simulations, ΔT_{fut} is set equal to $T_a(t) - T_a(0)$. For this, we use the continuation of the Climber-2 simulations forced by changes of parameters of the Earth’s orbit and by anthropogenic CO_2 emissions (Ganopolski et al., 2016). These emissions start in the year 1950 C.E. and proceed with a simulation-independent rate until the prechosen cumulative emission level E_{tot} is achieved. We chose two Climber-2 simulations: one with $E_{tot} = 1000$ PgC and another with $E_{tot} = 3000$ PgC, in which emissions cease in future years 100 and 300 correspondingly. Upon this, anthropogenic CO_2 emission rate is set to zero, and the Climber-2 simulation is continued with a freely evolving carbon cycle. Thereafter, our simulations based on the Climber-2 output with $E_{tot} = 1000$ PgC and $E_{tot} = 3000$ PgC are referred to as TR1000 and TR3000, respectively.

However, the sea floor warming might proceed in a much slower rate than the surface air warming (Lamarque 2008; Heuzé et al. 2015) except over the shallowest part of the shelf (up to a few metres, Dmitrenko et al. 2011; Bogoyavlensky et al. 2018, 2022; Overduin et al. 2019). Therefore, we performed one more, 'committed' simulation, in which future $T_a(t)$ is a repetition of the Climber-2-simulated $T_a(0)$ (corresponding to $\Delta T_{\rm fut} \equiv 0$). This simulation is thereafter referred to as TR0. In brief, our simulations represent a 'window of possibilities' with the temperature change in TR3000 (TR0) serving as an uppermost (lowermost) possible sea floor warming.

We note that there is a common belief that the seafloor temperature is rather insensitive to climate changes provided that the shelf is flooded. However, a quite comparable warming near the Arctic Shelf seafloor is simulated by at least a single model (ACCESS Earth System Model version 1.5, Fig. S3) in year 2300. In addition, very similar rates of the warmings of the surface air and at the sea floor are projected when the Arctic sea ice loss proceeds to a sufficient degree (Malakhova and Eliseev 2023). Thus, we conclude that the upper range of our seafloor warming is not a purely speculative.

Nonetheless, we highlight that anthropogenic emissions in TR1000 and TR3000 attempt to mimic neither historical emissions nor common scenarios for anthropogenic emissions in the future (e.g., Eyring et al. 2016). Nonetheless, taking into account that cumulative anthropogenic CO_2 emissions into the atmosphere for 1750-2004 are close to 500 PgC (Friedlingstein et al. 2020), one could loosely ascribe model year 50, when the cumulative emissions are close to this value, to year 2000 C.E. This ascription is not principal to our results, but might be helpful for putting the figured numbers into the context of the ongoing and future climate changes.

For future period, we neglect sea level changes on hydrostatic pressure. The impact of such assumption is discussed in Section 4. A neglect of pressure contribution is also characteristic for some of the other estimates of future methane hydrate response to climate changes (Buffett and Archer 2004; Hunter et al. 2013).

The value of the heat flux from the Earth's interior G is time-independent, but is varied between different simulations. Depending on simulation, we set it equal to either 45 mW m^{-2} or to 60 mW m^{-2} or to 75 mW m^{-2}. The intermediate of these values is characteristic for the most part of the Arctic shelf (Pollack et al. 1993; Davies 2013). In turn, value $G = 75$ mW m^{-2} is typical for rift zones. Regions with 45 mW m^{-2} are rare in the Arctic, but this value is still studied for completeness.

Our simulations fulfil important conditions which are necessary for a qualitatively realistic outcome. Namely, the present-day temperature is negative over the whole Arctic shelf (Fig. S2). Past changes of both permafrost layer and MHSZ follow the Pleistocene climate curve with some delay (Romanovskii et al. 2005; Malakhova and Eliseev 2017, 2018, 2020b, a). An example (for $G = 60$ mW m^{-2}) of the simulated permafrost layer and MHSZ for the whole period (from 400 kyr B.P. to 100 kyr A.P.) is shown in Fig. S6.

Methane content per unit volume of the sediments of the subsea hydrates is calculated following (Gornitz and Fung 1994; Biastoch et al. 2011; Majumdar and Cook 2018; Stranne et al. 2017)

$$\tilde{m}_{CH_4} = k_{CH_4} \rho_{CH_4} \phi \theta_{CH_4} \tag{1}$$

where the gas expansion coefficient from the sediment condition to the standard temperature and pressure (STP) is $k_{CH_4} = 140$, methane density at STP is $\rho_{CH_4} = 0.7168$ kg m^{-3}, and $\theta_{CH_4} = 0.05$ is a fraction of pore volume occupied by hydrates (Gornitz and Fung 1994; Buffett and Archer 2004; Klauda and Sandler 2005). Then, the total methane content per unit area of the sediments, m_{CH_4}, is calculated by integrating $\tilde{m}_{CH_4}$ over the estimated methane hydrate stability zone.

We highlight that, in our simulations, permafrost is assumed to exist in a sediment layer in a given year if the simulated temperature in this layer is below the freezing point for this year. While this criterion does not observe the water content of this layer, we note that in our simulations, the sediment pore space is assumed to be filled either by liquid water or by ice (Section S3).

Another term to be clarified is 'survival'. When applied to permafrost, this term means that the permafrost layer, which is formed earlier in a given simulation, continues to exist (probably with a different thickness). In a similar way, the term 'survival' is applied to MHSZ. Survivals of permafrost and MHSZ are studied separately—each is governed by its own criterion (temperature below the freezing threshold for permafrost and temperature-pressure conditions for MHSZ).

We highlight that the calculation of methane content in hydrates and methane release because of their dissociation is not a major goal of our paper. However, even the order-of-magnitude estimates for these values are instructive. We make these estimates in a very simple manner by calculating the release of methane from the sediments to the oceanic water based on dm_{CH_4}/dt Eq. 1. In this, we assume the following:

- Methane, which is released from the hydrate dissociation because of MHSZ shrinking, is instantly transported to the sediment–water interface but is subjected to chemical loss in the sulphate reduction zone. The latter loss is represented via coefficient $K_S < 1$.
- When MHSZ shrinks, both top and bottom boundaries contribute to the CH_4 release at the sediment–water

interface. In other words, we assume that the MHSZ is permeable for methane transport.

Thus, the sediment-to-ocean CH_4 flux per unit area reads

$$f_{CH_4} = K_S \frac{dm_{CH_4}}{dt}. \tag{2}$$

Coefficient K_S is set equal to the spatially uniform value of 0.5, which is adapted from the review paper by Ruppel and Kessler (2017).

We note that, in general, sulphate reduction is a rather complex process depending, in particular, on the rate of methane delivery to the sulphate reduction zone. Thus, our usage of a single coefficient to represent this process is a drastic simplification. However, because we do not account for explicit geography in our set up, we feel that our estimates are correct at least for the order of magnitude with this respect—it is clear that an apparent, mechanistically derived K_S can not be larger than unity, and it is likely to be of the same order of magnitude as 1/2.

Thereafter, we use f_{CH_4} for fluxes per unit area, while F_{CH_4} is used for area-cumulative fluxes. In a similar way, we use m_{CH_4} and M_{CH_4} for mass per unit area and for total mass in a specified region correspondingly.

3 Results

3.1 Permafrost

Similar to that obtained earlier with SMILES (Malakhova and Eliseev 2017, 2018, 2020b, a), the permafrost layer with thickness from 300 to 1200 m develops in the shallow and middle parts of the Arctic shelf to $t = 0$ (Fig. 1).

In the outer part, the thickness of this layer is $\leq$ 150 m owing to the shorter interval when the sediments are exposed to cold air temperatures during the marine regression. The only exception is case $\left(H_B = 100 \text{ m}; \; G = 75 \text{ mW m}^{-2}\right)$, in which permafrost disappears several kiloyears before this time instant. All this in a broad agreement with the observational results (Bogoyavlensky et al. 2022, 2023; Bukhanov et al. 2023), who showed that the permafrost in the Laptev Sea becomes sporadic or non-existent below the 60-m isobate. However, in the East Siberian Sea, it could exist at shallower depths. As it is expected, the permafrost layer thickness is larger for simulations with smaller contemporary shelf depth, which is at a longer contact with the atmosphere during oceanic regressions, and for simulations with a smaller geothermal heat flux. Among the studied cases, the largest present-day permafrost layer thickness, about 1200 m, is simulated for case $\left(H_B = 10 \text{ m}; \; G = 45 \text{ mW m}^{-2}\right)$.

After $t = 0$, the subsea permafrost thaws, both from the top and from the bottom. The bottom thaw is basi-

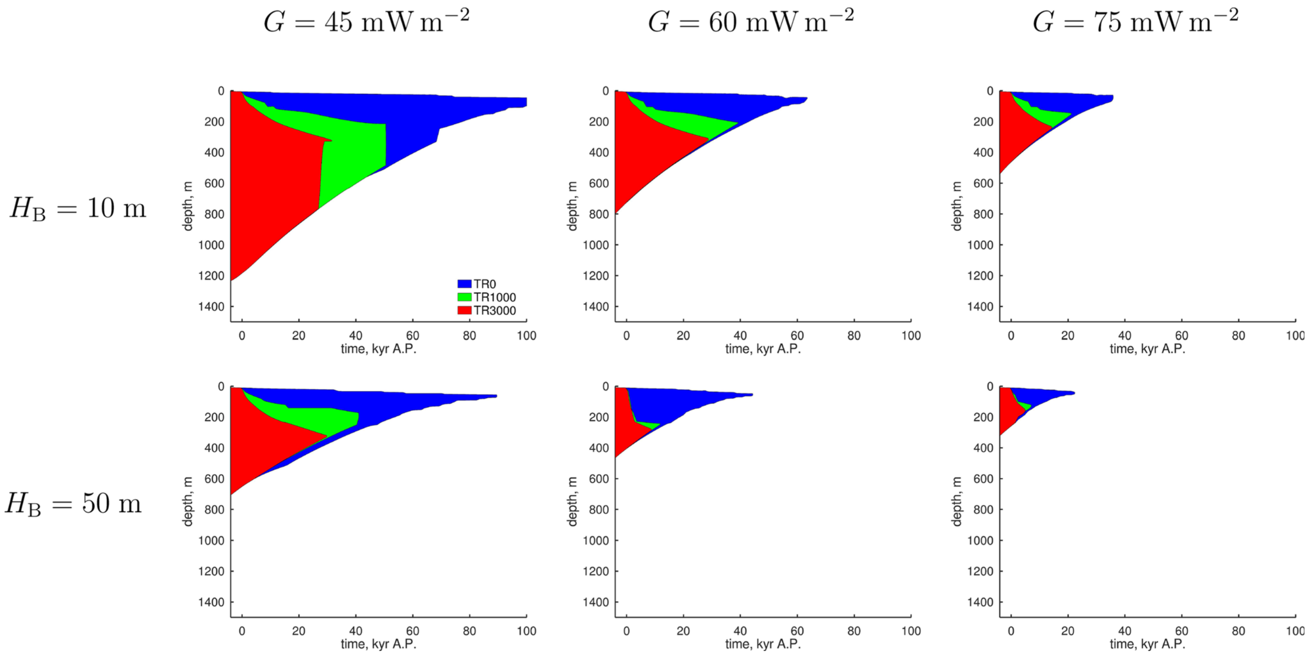

Fig. 1 Frozen sediment layers in different SMILES simulations (colours) as functions of time in future for $H_B = 10$ m and 50 m and different values of geothermal flux G. Ordinates show the depth below the sea floor. Boundaries of the frozen layer are smoothed with a window length of 1 kyr. Time instant $t = 0$ is formally ascribed to common year 1950

cally independent of applied warming scenario except at the outer shelf but depends on both G and H_B. If one averages the bottom thaw rate, $v_{\mathrm{pf,b}}$, for 0–1 kyr.A.P., the maximum value, $\approx 16.7\ \mathrm{m\,kyr^{-1}}$, is simulated for the shallow shelf. This value is in agreement with the measurement reported in Koshurnikov (2023). For this part of the shelf, the bottom thaw rate depends only weakly on geothermal heat flux intensity. For the middle shelf, the dependence of $v_{\mathrm{pf,b}}$ on G is more marked: this rate changes from $\approx 12\ \mathrm{m\,kyr^{-1}}$ for $G = 75\ \mathrm{mW\,m^{-2}}$ to $15\ \mathrm{m\,kyr^{-1}}$ for $G = 45\ \mathrm{mW\,m^{-2}}$. For most part of the permafrost degradation, the bottom thaw of the frozen layers is a continuation of the earlier thaw, which certainly is not related to CO_2 emissions, and is a long-term response to the onset of the Holocene (Malakhova and Eliseev 2017, 2020b). Further in the future, $v_{\mathrm{pf,b}}$ slows down.

The permafrost table thaw rate $v_{\mathrm{pf,t}}$, in contrast, most strongly depends on applied external CO_2 emissions into the atmosphere. As it is expected, the larger the emission rate, the faster the thaw. For TR0, this rate is always smaller than $\approx 1.5\ \mathrm{m\,kyr^{-1}}$ irrespective of G and H_B. Such values are quite similar to those exhibited before $t = 0$. A severalfold larger $v_{\mathrm{pf,t}}$, typically from about $2\ \mathrm{m\,kyr^{-1}}$ to approximately $13\ \mathrm{m\,kyr^{-1}}$, is simulated in TR1000 and TR3000 for $0 \le t \le 10$ kyr and, by and large, is independent of G. In turn, $v_{\mathrm{pf,t}}$ depends on H_B and on CO_2 emission rate, but in a complicated way because of the dependence of this rate on the state simulated for $t = 0$. In contrast to $v_{\mathrm{pf,b}}$, $v_{\mathrm{pf,t}}$ changes in time non-monotonically but still shows the above-mentioned dependencies on G and H_B. Orbital forcing, which is taken into account in simulations TR1000 and TR3000, leads to temporal retardations of the permafrost table thaw rate. However, its effect is not a dominant one, because such thaw (albeit with a much reduced rate) is exhibited in simulation TR0 as well.

Time before permafrost is extinguished at the Arctic shelf strongly depends on all parameters: contemporary shelf depth, geothermal heat flux, and CO_2 emission rate (left panels in Fig. 2). We note that, because in our simulations initial T_B is a function of H_B, the dependence of our results on contemporary shelf depth implicitly includes the respective dependence on initial near-floor water temperature.

For the outer shelf ($H_\mathrm{B} = 100$ m) permafrost is either disappears before $t = 0$ or is simulated to disappear during few centuries in the future provided that G is sufficiently large ($\ge 60\ \mathrm{mW\,m^{-2}}$ in our experiments). Only for the smallest employed value of the geothermal heat flux permafrost continues to exist in the future with the date of the complete degradation, $t_{\mathrm{pf,end}}$, which is 1 kyr A.P. for TR3000, 2 kyr A.P. for TR1000, and amounts to 11 kyr A.P. for TR0.

In the CO_2-emission forced runs and for the middle and shallow parts of the shelf, $t_{\mathrm{pf,end}}$ in our simulations is never smaller than 5 kyr A.P. In this part of the shelf and in the simulation with $G = 45\ \mathrm{mW\,m^{-2}}$, $t_{\mathrm{pf,end}}$ is as large as 32 kyr A.P. for TR3000 and even 51 kyr for TR1000. These values are again in agreement with those reported by Archer (2015).

The longest survival of the subsea permafrost is simulated in runs TR0 in the middle and shallow parts of the shelf. In these experiments, $t_{\mathrm{pf,end}}$ is ≥ 22 kyr A.P. or even survives till the end of the simulation.

All our simulations show a clear dependence of $t_{\mathrm{pf,end}}$ on geothermal heat flux: the larger the flux is, the sooner the subsea permafrost ceases to exist. This is an obvious consequence of the respective dependence of $v_{\mathrm{pf,b}}$. The dependence of $v_{\mathrm{pf,t}}$ on future CO_2 emission rate leads to the negative correlation of $t_{\mathrm{pf,end}}$ with the applied cumulative emissions. In addition, the time of the subsea permafrost disappearance is smaller for larger H_B because the larger present-day shelf depth leads to a thinner permafrost layer at $t = 0$.

3.2 Methane hydrate stability zone

The methane hydrate stability zone ceases to exist before the present at the outer shelf ($H_\mathrm{B} = 100$ m; Fig. 3). This is in agreement with our previous simulations (Malakhova and Eliseev 2017, 2018, 2020b, a) which were driven by other forcing datasets. For the middle and shallow parts of the shelf in all our simulations, the present-day MHSZ base is located deeper in the sediments than its permafrost counterpart. This is due to the impact of the hydrostatic pressure of the water. We note, however, that this impact is only possible in the presence of the overlying permafrost layer—otherwise, MHSZ does not form at all. In turn, the MHSZ top depth is larger than the permafrost top depth for the same pair (H_B; G). For the middle and shallow parts of the shelf, MHSZ bottom is located at the about 1400 m below the sea floor for $G = 60\ \mathrm{mW\,m^{-2}}$ and about 900 m for $G = 75\ \mathrm{mW\,m^{-2}}$. In the outer shelf, methane hydrate stability zone disappears before $t = 0$ (Fig. 2).

The rate of the MHSZ shrinking from the bottom, $v_{\mathrm{MHSZ,b}}$, averaged from $t = 0$ to $t = 1$ kyr A.P. amounts from $13\ \mathrm{m\,kyr^{-1}}$ to $30\ \mathrm{m\,kyr^{-1}}$ depending on H_B and on G, which is similar to its permafrost counterpart. Again, MHSZ shrinking from the bottom is a continuation (albeit slightly fastened) of the corresponding shrinking during the last few millennia before the onset of the external CO_2 emissions. Later on, $v_{\mathrm{MHSZ,b}}$ magnitude increases. For instance, its vertical movement rate may be as large as about $100\ \mathrm{m\,kyr^{-1}}$ for a number of simulations with $H_\mathrm{B} = 50$ m. Interestingly, in simulations with the moderate geothermal heat flux $G = 60\ \mathrm{mW\,m^{-2}}$, such large values of $v_{\mathrm{MHSZ,b}}$ are exhibited only in the TR3000 simulation. In the simulations with other values of G, the rate of $v_{\mathrm{MHSZ,b}}$ averaged over 5 kyr A.P. $\le t \le$ 10 kyr A.P. is close to $100\ \mathrm{m\,kyr^{-1}}$ for all three emission scenarios.

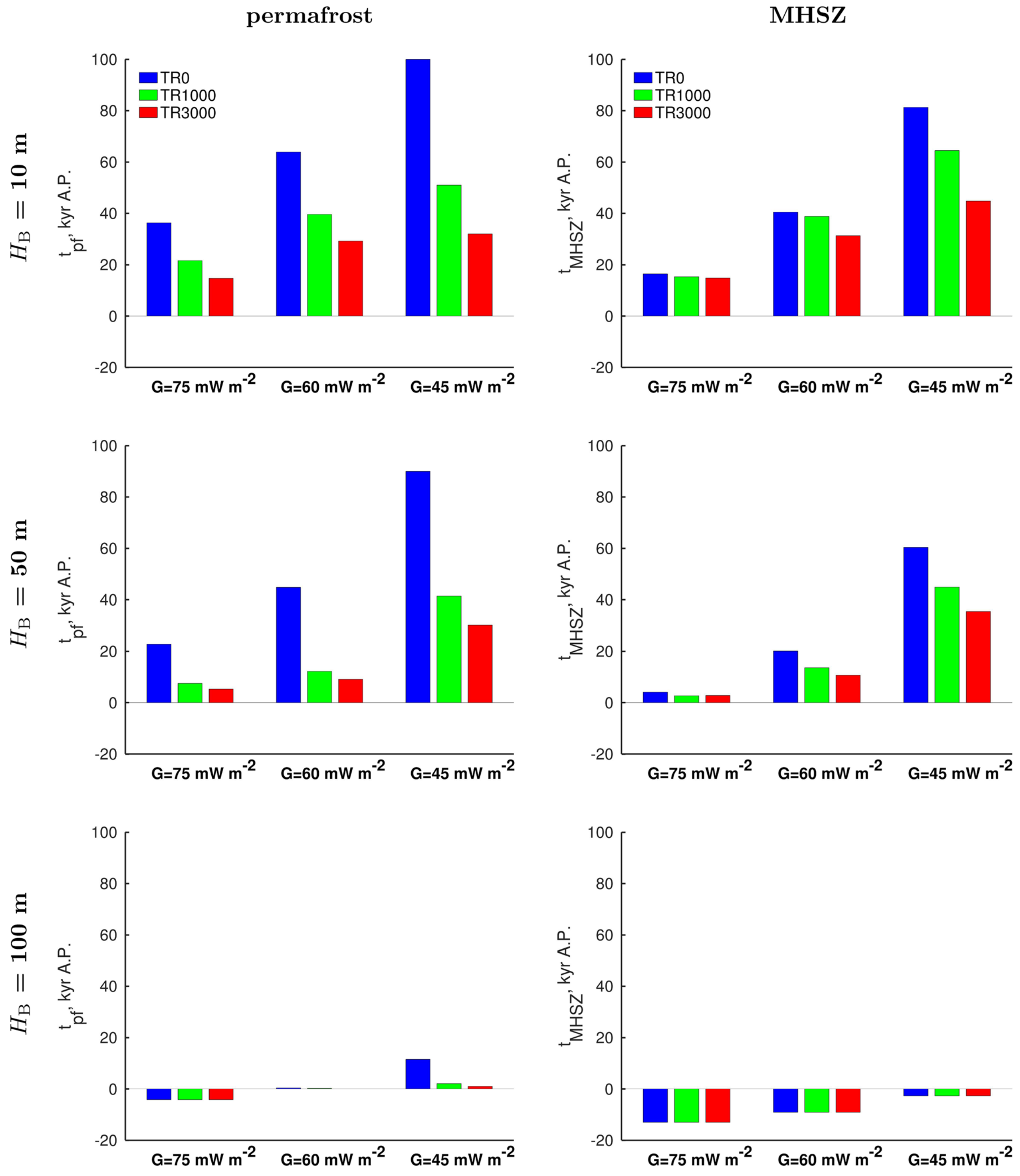

Fig. 2 Time of the disappearance of permafrost (left) and of the methane hydrates stability zone (right) for different H_B. Negative time instants indicate that the feature under study disappears before $t = 0$. Value 100 kyr A.P. indicates that permafrost survives till the end of the simulation. Time instant $t = 0$ is formally ascribed to common year 1950

The methane hydrate stability zone, similar to that exhibited for permafrost, shrinks from the top at a much slower rate. On the shallow and middle parts of the shelf and during the first 1 kyr after the emission onset, this rate, $v_{\mathrm{MHSZ,t}}$, changes from 0 to 6 m kyr^{-1} depending on contemporary shelf depth, geothermal heat flux, and emission scenario. The MHSZ top deepening is not a continuation of the tendency during the last few millennia before $t = 0$—in fact, before the emission onset, MHSZ top shallows rather than deepens at these parts of the shelf in all our simulations. Later on, $v_{\mathrm{MHSZ,t}}$ increases. For the last few millennia before the complete disappearance of the methane hydrate stability zone, it may be of the order of 100 m kyr^{-1} (Fig. 3).

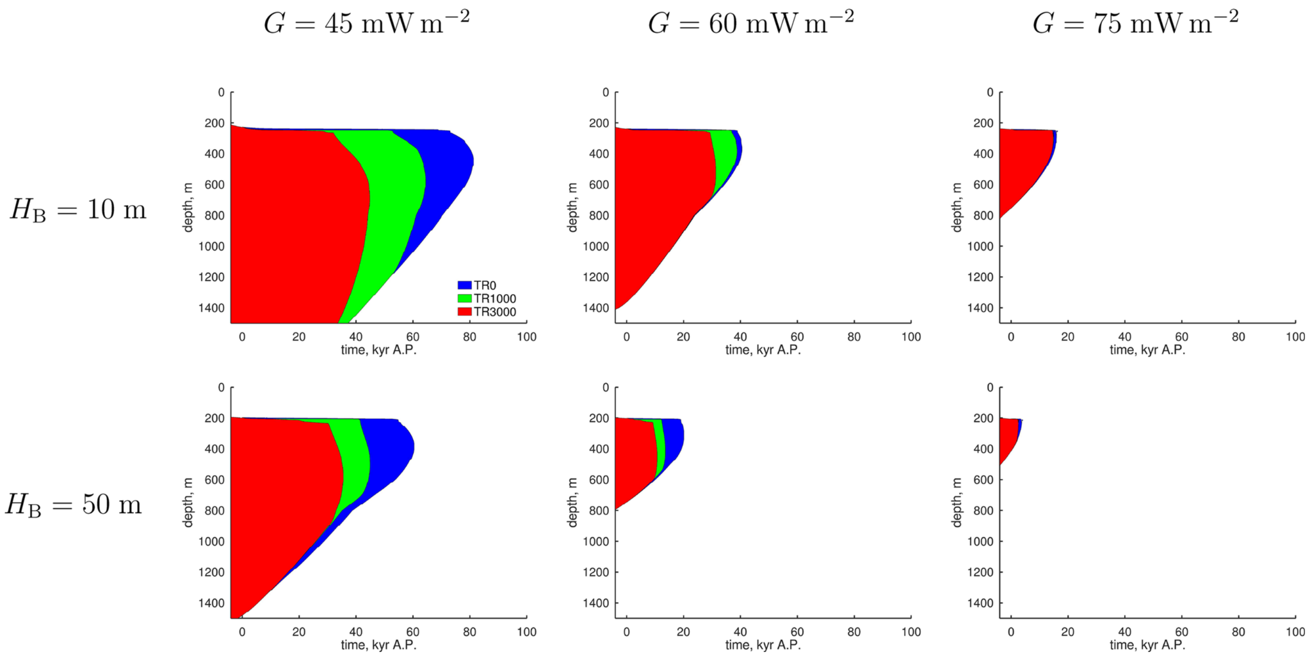

Fig. 3 Methane hydrate stability zone in different SMILES simulations (colours) as functions of time in future for $H_B = 10$ m and 50 m and different values of geothermal flux G. Ordinates show depth below the sea floor. Time instant $t = 0$ is formally ascribed to common year 1950

The time since the emission onset till the complete MHSZ disappearance (time instant $t_{\mathrm{MHSZ,end}}$) at the shallow and middle parts of the shelf in our simulations is from 3 kyr for $\left(H_B = 50 \text{ m};\ G = 75 \text{ mW m}^{-2}\right)$ in both runs TR1000 and TR3000 (Fig. 2). For the same pair (H_B; G), it is of the same order of magnitude (4 kyr) in run TR0. However, in other simulations, $t_{\mathrm{MHSZ,end}}$ is located markedly further in the future. For $G = 60$ mW m^{-2} and $H_B = 50$ m ($H_B = 10$ m), $t_{\mathrm{MHSZ,end}}$ changes from 11 to 20 kyr A.P. (from 31 to 41 kyr A.P.) depending on the applied CO_2 scenario. For small geothermal heat flux $G = 45$ mW m^{-2}, this time instant is from 36 to 81 kyr. A.P. depending on CO_2 scenario and on contemporary shelf depth. Basically, $t_{\mathrm{MHSZ,end}}$ is negatively correlated with both G, H_B and with the rate of the CO_2-induced warming in the atmosphere.

A comparison between left and right panels in Fig. 2 shows that, for a given H_B, G, and emission scenario, MHSZ disappears earlier than the respective permafrost layer. However, we did not find a systematic dependence for the difference between these two extinction times on the above-listed parameters.

3.3 Methane release from the sediments to the water

The values of averaged over the prechosen time intervals are shown in Fig. 4. For 'recent past' (the last millennium $t = 0$) for both shallow and middle parts of the shelf is between 0.3 and 5.2 gCH$_4$ m^{-2} yr^{-1}. In simulation TR0, f_{CH_4} may either increase or decrease during the next 2 kyr depending on H_B and G. In contrast, future enhancement of the MHSZ shrinking from the top in simulations with external CO_2 emissions always leads to an increase of this flux during 1 or 2 kyr with subsequent decrease thereafter. In particular, the means of f_{CH_4} over 0.5-1 kyr A.P. in these model runs typically amount from 4 to 16 gCH$_4$ m^{-2} yr^{-1} at the shallow and intermediate shelves (except for $G = 45$ mW m^{-2} which is accompanied by much smaller values of f_{CH_4}).

We note that our f_{CH_4} estimates for time interval from −0.5 kyr A.P. to +0.5 kyr.A.P. are within the corresponding range as measured at the shallow and intermediate parts of the shelf by Shakhova et al. (2019) (≤ 10 gCH$_4$ m^{-2} yr^{-1} in our units and taking into account impacts of an initial degree of subsea permafrost thaw and by modern methanogenesis combined with partial release of preformed CH_4 from interpore and/or relic hydrates preserved within the permafrost at the shallow and intermediate shelves).

4 Discussion and conclusions

4.1 Summary

We performed simulations with the SMILES (the Sediment Model Invented for Long-tErm Simulations) for 100 kyr in future. These simulations were initialised from the state obtained for a broadly defined 'present-day state' and forced by surface air temperature (SAT) changes as simulated by

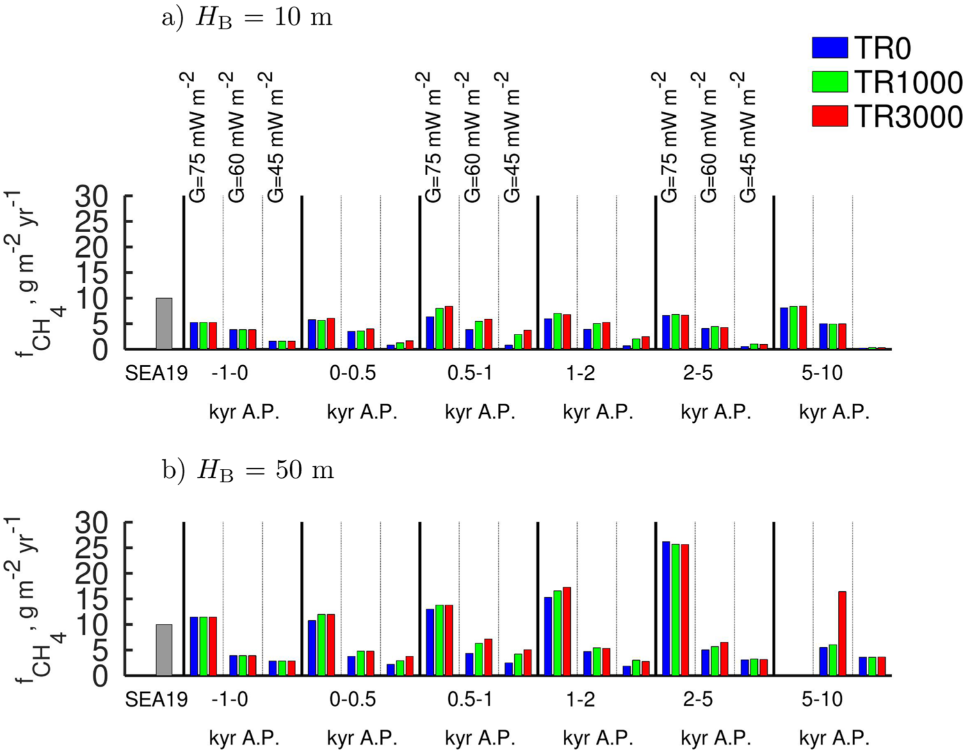

Fig. 4 Methane flux from the sediments to the ocean averaged over different time intervals. The grey rectangle which is labelled as 'SEA19' is a value reported in the review by Shakhova et al. (2019) taking into account impacts of an initial degree of subsea permafrost thaw and by modern methanogenesis combined with partial release of preformed CH_4 from inter-pore and/or relic hydrates preserved within the permafrost at the shallow and intermediate shelf. Time instant $t = 0$ is formally ascribed to common year 1950

the Climber-2 Earth system model. In turn, SAT changes in Climber-2 were modelled as a response to idealised scenarios of CO_2 emissions and to changes of the parameters of the Earth's orbit. Because of uncertainty in relating SAT changes to changes of temperature at the surface of the oceanic shelf sediments, T_B, we used a broad interval of future T_B changes: from no change since the present day (which is a continuation of the Holocene history) to the change with the same rate as it is simulated for SAT. Owing to additional uncertainty due to existing spatial variations of geothermal heat flux, we repeated model runs for several values of this variable ranging from 45 to 75 mW m^{-2}. We neglected the possible impact of the sea level on freeze/thaw temperature and on thermodynamic stability of methane hydrates.

We found that, for the outer shelf ($H_B = 100$ m), permafrost either disappears before $t = 0$ or is simulated to disappear during a few centuries in future provided that $G \geq 60$ mW m^{-2}. For smaller G and at the same part of the shelf, the date of the complete degradation is not later than 11 kyr A.P. depending on the applied emission scenario. For the middle and shallow parts of the shelf, in the CO_2-emission forced runs the subsea permafrost survives, at least, for 5 kyr after the emission onset or even much longer. Without applied greenhouse forcing, the permafrost exists here at least until 22 kyr A.P. or even survives till the end of the model runs.

At the shallow and middle parts of the shelf in our simulations methane hydrate stability zone disappears not earlier than at $t = 3$ kyr A.P., but typically MHSZ survives until 11 to 20 kyr A.P. (from 31 to 41 kyr A.P.) for $G = 60$ mW m^{-2} and $H_B = 50$ m ($H_B = 10$ m). For smaller geothermal heat flux $G = 45$ mW m^{-2}, the time instant of the local MHSZ extinction is from 36 to 81 kyr A.P. depending on the CO_2 scenario and on the contemporary shelf depth.

Timings of local extinction of both the subsea permafrost and MHSZ are negatively correlated with the geothermal heat intensity provided that other factors are being equal. This reflects the strong control which this variable sets on the permafrost thaw from the bottom and the corresponding MHSZ shrinking. In turn, thaw from the top and MHSZ table deepening is basically determined by the applied CO_2 forcing scenario. Because of different contribution of processes at the top and bottom boundaries to total loss both for permafrost and for MHSZ, the timings of the permafrost disappearance depend stronger on the applied scenario relative to that of the MHSZ extinction.

The most important impact of the future orbital forcing is a non-monotonic change of T_B. Its impact on simulations is more important for the permafrost than for MHSZ. In particular, it leads to retardation of the permafrost table thaw rate in TR1000 and TR3000. However, its effect is not a dominant one, because such thaw (albeit with a much reduced rate) is exhibited in simulation TR0 as well.

Owing to multi-millennium timescale of the variations of the parameters of the Earth's orbit, our scenario TR0 during the next several millennia is similar to the future scenario employed by Matveeva et al. (2020). In this respect, it is remarkable that the timescale of the MHSZ extinction is very similar between our paper and the paper by Matveeva et al. (2020). It credits an additional support for our results.

4.2 Implications for pan-Arctic

Despite of very rudimentary account of geographically distributed properties, it is instructive to estimate the pan-Arctic values of the above-studied variables. Thus, we integrated our simulated variables over the whole Arctic shelf with a crude approximation for such integrals: we assume that our shallow shelf is representative for all shelf areas with $H_B \leq 30$ m, our intermediate shelf—for $30 \text{ m} < H_B \leq 75$ m, and our deep shelf—for $H_B > 75$ m. To partly compensate for our rudimentary geography, we limit these integrals to the regions where the subsea permafrost was simulated in a more realistic setup (Malakhova 2020) (supplementary Section S4.4), in which the geographically explicit surface forcing was used (supplementary Fig. S8 and Table S4)—just by multiplying vertical integrals by the area of such regions. We note that the geographical distribution of the subsea permafrost in the Arctic simulated by Malakhova (2020) is in general agreement with an alternative simulation (Overduin et al. 2019). We also assume that MHSZ develops only in the subsea permafrost and covers the whole permafrost-bearing region as simulated by Malakhova (2020). In addition, we acknowledge the following important caveats in our 'pan-Arctic' calculations:

- Geological features are neglected completely. Such features may lead either to local variations of the geothermal heat flux or to release of the thermogenic methane from the sediments.
- In our simulations, we use the Climber-2 surface air temperature anomaly from the present day only for the grid cell corresponding to the East Siberian Arctic shelf to for our model. This anomaly is apparently different even from temperature in other model grid cells. However, three shelf regions are located in nearby grid cells (recall very coarse zonal resolution of Climber-2, $\approx 51^o$), and temperature anomaly in our preselected Climber grid cell deviates from its zonal mean counterpart no more than by 20% during the most part of the simulation (supplementary Section S3 and Fig. S4).
- Moreover, we use geographically uniform value ($-12^o C$) for the reference temperature for the top boundary of the shelf exposed to the atmosphere during marine regressions. The Climber-simulated anomalies are added on top of this reference temperature (supplementary Section S3). This caveat is partly (albeit far from completely; see below) ameliorated by using the above-mentioned subsea permafrost extent adapted from Malakhova (2020).

We these caveats in mind, we highlight that our calculations for methane stocks and for methane fluxes are correct, at best, only for an order of magnitude.

In addition, because of the aforementioned limitations, we do not make attempt to calculate the present-day volumes of the subsea permafrost and of the permafrost-associated methane hydrate stability zone—both of them may be sensitive to the local geological features—and present only changes relative to the present day.

The subsea permafrost volume, V_{pf}, is decreased by 1.3% (4.5%, 6.8%) during the first 0.5 kyr in future in simulation TR0 (TR1000, TR3000) with $G = 60 \text{ mW m}^{-2}$ (Fig. 5a). Larger permafrost volume loss during the same time interval is simulated with $G = 75 \text{ mW m}^{-2}$: 2% (10%, 13%). At $t = 1$ kyr A.P., V_{pf} in simulations TR0 is decreased by 1.5–4.6% relative to $t = 0$ depending on G, by 4–14% in simulations TR1000, and by 8–20% in simulations TR3000. Our estimates are markedly smaller than those reported by Wilkenskjeld et al. (2021) who claimed that 35% of the initial subsea permafrost volume is lost by common era year 3000 under high-emission scenario SSP5−8.5. While our and their modelling setups are pretty different because of (i) differences in emission scenarios, (ii) their usage of the Max-Planck-Institute (MPI) oceanic model to generate the temperature at top of the sediments rather than our simple transfer of the near-surface atmospheric temperature anomaly to the sediment-oceanic interface, (iii) an explicit treatment of the geographic features in their simulations and a very rudimentary account for them in ours, (iv) their usage of 'partially frozen cells' (such partial freezing is neglected in our setup), and (v) an incomplete correspondence between our calender and the common era calender; the difference is still very marked. We note that they are unlikely to be ascribed to the driving Earth System Models (ESMs) owing to comparable equilibrium climate sensitivities (2.8 K) and transient climate responses (1.8 K) between MPI-ESM employed by Wilkenskjeld et al. (2021) and Climber-2 used in our exercise (MacDougall et al. 2020). The most likely reason (as pointed out to us by S. Wilkenskjeld) is their implementation of 'partially frozen cells' leading to a smaller amount of ice in the sediment layers, which are located deeper than 100 m relative to the sea floor. Thus, melting the pore ice in the upper part of the sediment leads to larger relative loss of the permafrost volume in simulations by Wilkenskjeld et al. (2021) relative to that in our simulations.

After 10 kyr after time instant $t = 0$ (corresponding to the emission onset for TR1000 and TR300), in our simulations, the subsea permafrost volume loss is, depending

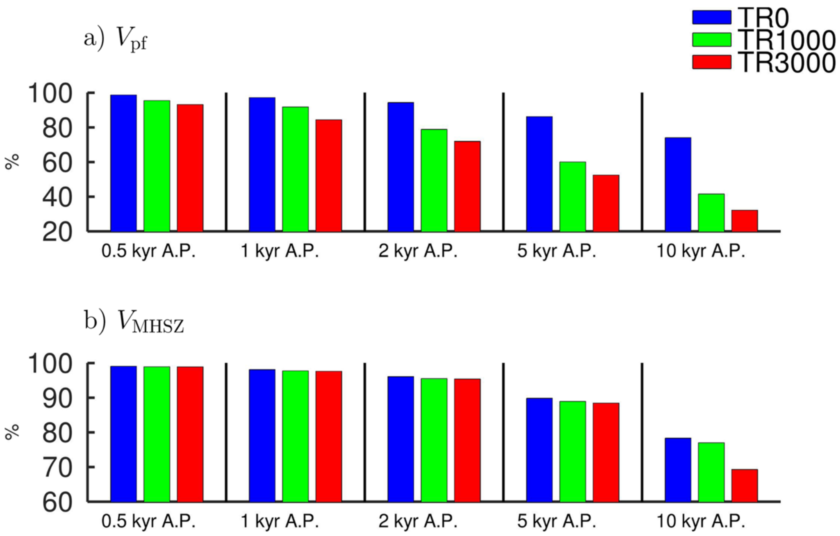

Fig. 5 Volume of the subsea permafrost (**a**) and the permafrost-associated subsea methane hydrate stability zone (**b**) relative to the time instant of the CO_2 emission onset (which is formally ascribed to common year 1950) in simulations with $G = 60$ mW m^{-2} averaged over the whole Arctic shelf

on G, 16–44% in simulations TR0, 27–75% in simulations TR1000, and 37–86% in simulations TR3000. In this as well as in previously studied time slices, the largest V_{pf} loss is exhibited for $G = 75$ mW m^{-2} and the smallest one is for $G = 45$ mW m^{-2}.

In contrast to the subsea permafrost volume, the perma frost-associated MHSZ loss depends more weakly on the applied emission scenario (Fig. 5b) but strongly depends on G. This is again consistent with the finding that MHSZ mostly shrinks from below rather than from above. The pan-Arctic methane hydrate stability zone volume, V_{MHSZ}, is reduced by 0.4–3.4% during the first 0.5 kyr after the CO_2 emissions onset, by 1.0–7.8% during the next 0.5 kyr, by 2–16% to $t = 2$ kyr A.P., by 4–45% to $t = 5$ kyr A.P., and by 8–60% to $t = 10$ kyr A.P. relative to its value at $t = 0$. Similar to that already exhibited for V_{pf}, the largest V_{pf} loss is exhibited for $G = 75$ mW m^{-2} and the smallest one is for $G = 45$ mW m^{-2}. Our estimate of the relative V_{MHSZ} loss for $G = 60$ mW m^{-2} during the first 1 kyr after the emission onset is similar to that obtained by Hunter et al. (2013) in their high-emission scenario ECP8.5 despite they do not model the permafrost-associated methane hydrates.

Geothermal heat flux is also very important for setting the present-day simulated pan-Arctic methane stock, M_{CH_4}, in the subsea hydrates. This stock is equal to 1230 $PgCH_4$ (all values for this variable are rounded to the nearest integers) in simulations with $G = 60$ mW m^{-2} (Fig. 6a), but it is as half as much (635 $PgCH_4$) in simulations with $G = 75$ mW m^{-2} and is larger by about 1/3 (1695 $PgCH_4$) in simulations with $G = 45$ mW m^{-2}. The majority of this stock (from 63 to 71% depending on G) is in the East Siberian Arctic Shelf (ESAS), with smaller contributions from the West Eurasian and from the North American Arctic Shelves (17–20% and 11–17% correspondingly; for shelves definition, see supplementary Fig. S7). The total pan-Arctic stock is broadly consistent with the values reviewed by James et al. (2016) who figured out that up to 1400 $PgCH_4$ may be stored in the submerged permafrost in the Arctic shelf. However, our estimate is an order of magnitude larger than that reported by McGuire et al. (2009) (≤ 65 $PgCH_4$).

The likely reasons for obtaining our value are (i) an assumption that hydrates exist everywhere in the MHSZ while Xu and Ruppel (2022) and Mestdagh et al. (2017) pointed out the hydrates are mostly absent in the uppermost part of MHSZ, and they exist in the lowermost part only provided that CH_4 flux from below is large enough, (ii) possible unfrozen (and, thus, unable to support the thermodynamic conditions for hydrate formation) subgrid-scale horizontal regions. Both assumptions might lead to the several-fold overestimated methane stock, and in combination, they might lead to the corresponding overestimate by order of magnitude.

We note a strong dependence of the methane stock on G, quite similar to that obtained in the present paper, was earlier simulated by Archer (2015) for ESAS, but with more moderate values of M_{CH_4} at this shelf (for instance, 846 $PgCH_4$ for $G = 60$ mW m^{-2}, while his estimates are typically ≤ 90 $PgCH_4$), likely owing to his accounting for the CH_4 dissolved content in the pore water.

Similar to that exhibited for MHSZ, the loss of the M_{CH_4} only weakly depends on the applied emission scenario during the first several kiloyears after the emission onset (Fig. 6a), despite there is a strong corresponding dependence on G. By design, our estimate of the relative methane hydrate stock decrease is identical to those obtained for the methane stability zone volume.

In contrast to MHSZ volume and its methane hydrate stock, the pan-Arctic methane flux from the sediments to the oceanic water, F_{CH_4}, exhibits slightly non-monotonic dependence on G. For instance, for last 0.5 kyr before $t = 0$, this

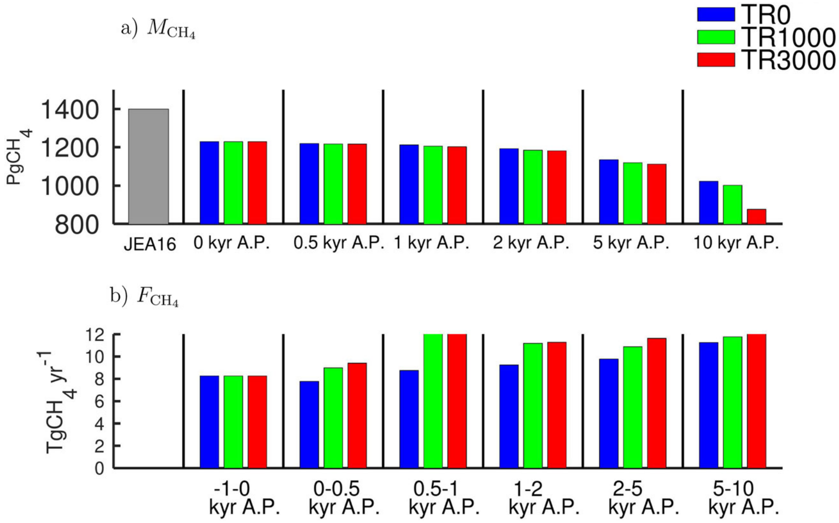

Fig. 6 Methane stock in the pan-Arctic permafrost-associated shelf hydrate (**a**) and CH_4 flux from the Arctic shelf sediments to the oceanic water in simulations with $G = 60$ mW m^{-2} (**b**). The grey rectangle with the label 'JEA16' in **a** stands for the empirically-based upscaling range as reviewed by James et al. (2016). Time instant $t = 0$ is formally ascribed to common year 1950

flux is 1.8 $\mathrm{TgCH_4\,yr^{-1}}$ for $G = 60$ mW m^{-2} (Fig. 6b). It is slightly larger, 1.9 $\mathrm{TgCH_4\,yr^{-1}}$, for the largest studied $G = 75$ mW m^{-2}, and is again larger, 2.40 $\mathrm{TgCH_4\,yr^{-1}}$, for the smallest studied $G = 45$ mW m^{-2}. The major contribution is from the East Siberian Arctic Shelf: for the last 0.5 kyr before the CO_2 emission onset and for the first 0.5 kyr after this onset, the flux from the sediments to the water from this shelf is from 1.3 to 3.4 $\mathrm{TgCH_4\,yr^{-1}}$ which is larger than the estimate by Archer (2015), who reported that in his simulations $F_{\mathrm{CH_4}}$ from ESAS is ≤ 0.4 $\mathrm{TgCH_4\,yr^{-1}}$. The likely reason for this difference is due to (i) an order-of-magnitude smaller methane stock in the ESAS sediments in his simulations compared to ours and (ii) his accounting for future sea level rise on MHSZ extent (warming scenario in Archer (2015) corresponds to the sea level rise ≥ 70 m at the time of peak warming).

Future changes of $F_{\mathrm{CH_4}}$ depends on G as well. If no CO_2 emissions are applied (TR0), this flux steadily increases during the next several kiloyears. In simulations with CO_2 emissions applied, $F_{\mathrm{CH_4}}$ increases, sometimes by an order of magnitude. For instance, in simulation TR3000 with $G = 60$ mW m^{-2}, even the being averaged over 0.5-1 kyr A.P., this flux is as large as 5.3 $\mathrm{TgCH_4\,yr^{-1}}$ (Fig. 6b); a higher counterpart value, 6.6 $\mathrm{TgCH_4\,yr^{-1}}$, is obtained in simulation TR3000 with $G = 75$ mW m^{-2}.

Thus, we conclude that the CO_2-induced warming in our simulations enhances the pan-Arctic subsea permafrost loss during 1 kyr after the emissions onset by several times. However, this warming is much less important for the respective MHSZ loss. Our estimates of methane release from the sediments to the oceanic water per unit area are consistent with existing respective estimates attributed to the subsea permafrost thaw. Our corresponding pan-Arctic estimate averaged over centennial or millennium time intervals typically never exceeds 14 $\mathrm{TgCH_4\,yr^{-1}}$ during few millennia from $t = 0$.

We did not make an attempt to estimate the corresponding release of methane from the oceanic water to the atmosphere because this is complicated by (i) methane oxidation in the water column, (ii) sea ice blocking of gas transport from the ocean to the atmosphere, and (iii) additional CH_4 sources unrelated to the methane hydrate dissociation, e.g., due to methanogenesis in the river mouths or in the submerged Yedoma or owing to release of the thermogenic methane (Archer 2007; James et al. 2016; Ruppel and Kessler 2017; Dean et al. 2018; Shakhova et al. 2019; Ruppel and Waite 2020). Assessing item iii is beyond the scope of the present paper. For items i and ii, it is clear that they could only diminish CH_4 flux at the ocean–atmosphere interface relative to its counterpart at the sediment-ocean interface. Malakhova and Golubeva (2022) reported that this difference may be as large as one order of magnitude provided that sea ice cover is similar to the present-day one. While the latter assumption seems unlikely for time instants after several decades from the present day, when most state-of-the-art climate models project an ice-free Arctic in summer under high-emission scenarios (Fox-Kemper et al. 2021), a severalfold decrease of methane flux at the ocean–atmosphere interface relative to the flux at the sediment-ocean interface still seems reasonable. We suggest that CH_4 flux at the ocean–atmosphere interface could not be larger than few $\mathrm{TgCH_4\,yr^{-1}}$. Thus, despite our pan-Arctic $F_{\mathrm{CH_4}}$ is substantially larger than estimated by Archer (2015), we agree (even with our likely overpredicted CH_4 stock in the Arctic shelf sediments) with his conclusion that methane hydrate dissociation in the subsea sediments can not support large estimates which were claimed recently (e.g., up to 17 $\mathrm{TgCH_4\,yr^{-1}}$, Shakhova et al. 2010). The same conclusion was made in the recent IPCC assessment (Canadell et al. 2021) (see also Berchet et al. 2016).

4.3 Uncertainties and limitations

We acknowledge the limitations of our study:

- In our simulations, we neglected the impact of future sea level (SL) rise on the thermodynamic stability of methane hydrates and on the freeze/thaw temperature of sea water. For both effects, this is true provided that the eustatic sea level rises only due to thermal expansion. However, it overlooks possible contribution to the sea level rise due to the melting of ice sheets. For instance, the recent IPCC Working Group 1 Assessment Report concluded that ice sheets melting may contribute as large as 40 m to sea level within a few centuries from now (Fox-Kemper et al. 2021). Nonetheless, ice sheets do not melt in the future in the Climber-2 simulations used here, and their contribution to the future SL rise is zero. In addition, if ice sheet melting to SL change is substantial, it would only enhance the thermodynamic stability of methane hydrates, thus shifting the dates of MHSZ extinction even further in the future. However, the hydrostatic pressure increase would decrease freeze/thaw temperature (supplementary Eq. S5), which would promote a faster response of the subsea permafrost to future warming.
- An important caveat is due to the lack of mechanistic biogeochemistry in our model reflected in vertically and geographically uniform θ_{CH_4}. This simplification may affect our results in two ways. First, it directly affects the estimated methane release. Second, it overlooks a negative feedback between the dissociation of methane hydrates and the amount of dissolved methane in pore volume (Ruppel and Waite 2020). The first effect is difficult to quantify in our setup. The second effect may only slow sown the hydrate dissociation, thus diminishing the release of methane and shifting the extinction of methane hydrates in the sediments further in time.
- As it was stated in Section 2, we neglected the heat released during dissociation of hydrates (Stranne et al. 2016). On one hand, the latent heat of hydrate dissociation leads to retardation of their response to climate change. Thus, it would only prolong the MHSZ existence in our simulations. However, on the other hand, accounting for this latent heat would suppress the formation of methane hydrates during Pleistocene glaciations as well. Provided that other things are equal, thinner MHSZ apparently would disappear earlier. It was shown by Stranne et al. (2016) and by Arzhanov and Malakhova (2023) that the former effect dominates and accounting for the latent heat of hydrate dissociation retards the disappearance of MHSZ under global warming. The latter even strenghtens our conclusions about the future fate of the sunsea permafrost and PAMH MHSZ. To account for this effect in a mechanistic fashion, one needs either data on methane hydrate saturation within MHSZ (such large-scale data are lacking) or to model their geochemistry. We plan to extend our model accordingly and to perform the relevant simulations in a future paper.
- As a continuation of the previous item, we note that, despite the specific heat of methane hydrate phase transition is 1.5-fold larger than ice/water phase transition, it is not so important at large scales. This is because at these scales, hydrate saturation is much smaller than unity (typically, $\theta_{\mathrm{CH}_4} = 0.05$, Gornitz and Fung 1994; Buffett and Archer 2004; Biastoch et al. 2011; Klauda and Sandler 2005), and its product with the ratio between the just mentioned latent heats (1.5) is much smaller than unity as well. An order-of-magnitude larger saturations is necessary to make the impact of the latent heat of hydrate dissociation comparable with the respective impact of the latent heat of ice/water phase transition. The layers with much higher hydrate saturation exist in the sediments, e.g., in Beaufort–Mackenzie Basin where this saturation could be as large as 60% (e.g., Majorowicz et al. 2012). However, such layers are at most several metres thick, and they are separated by the layers which contain little or no hydrate (Boswell et al. 2011).
- In principle, thermodynamic potentials may be used to improve estimates of m_{CH_4} and f_{CH_4} even in our setup. However, we feel that the major uncertainty of our estimates for methane stock and for methane fluxes is due to the neglect of the vertical and horizontal variations of hydrate saturations and due to the very simplified treatment of the impact of the sulphate reduction zone on these fluxes rather than due to the neglect of the respective latent heat of their formation and dissociation. Again, a full geochemistry model is necessary to pursue this goal.
- An additional uncertainty in our estimates is due to a complete neglect of the spatial inhomogeneity of most input parameters for our model. This includes both horizontal and vertical (and, plausibly, time variations of such even temporal on our 100-kiloyear time horizon). While some parameters are available at the horizontal grid (say, the present-day near-seafloor temperature (Bogoyavlensky et al. 2018) or the geothermal heat flux (Pollack et al. 1993; Davies 2013), most of them are lacking—especially, mineral and granulometric contents of the sediment down to the depth of 1.5 km. In particular, vertical layering of any input parameters could change our results, at least quantitatively. Such extension would be an important path in the development of our knowledge on the future fate of the thermal state of the subsea sediment. However, this is unfeasible at the date. Lacking the

respective data, we decided to perform our simulations in an idealised way but with a stratification relative to the contemporary H_B. We highlight that our setup and a general complexity of our model are quite comparable to other models of similar functionality, say with the models by Archer (2015) and by Matveeva et al. (2020).

- Partly, our neglect of geography is ameliorated by the large-scale structure of the forcing data—the anthropogenically induced climate changes have a very broad (basically, the pan-Arctic) scale. For our pan-Arctic scale, the neglect of geography is ameliorated (albeit, incompletely) by using the permafrost map by Malakhova (2020) to scale the local estimates. This map was obtained taking into account spatial variations of G—thus, implicitly taking into account geological features. The latter approach is very similar to that employed by Overduin et al. (2019).
- We used very idealised scenarios of CO_2 emissions leading to the 'calender uncertainty' in our simulations. For instance, simulations TR1000 and TR3000 assume a constant CO_2 emission rate during either 100 or 300 years with an abrupt decline to zero thereafter. This is in apparent contrast with the real-world emissions, which (i) started about two centuries earlier (around the mid-eighteenth century taking into account the sizeable land use change emissions) and (ii) proceed with a very non-uniform rate during the historical period. Moreover, emissions of other anthropogenic greenhouse gases (CH_4, N_2O, etc.) are ignored in the Climber simulations as well as possible natural climate drivers (e.g., volcanic eruptions, total solar irradiance changes). Further, possible natural climate variability is not simulated by Climber and, therefore, is ignored as well. In addition, other external forcings are neglected completely except the orbital one. We note, however, that long time scales involved in the problem at hand suppress the possible impact of scenario details on the obtained results. At least, the major finding related to the major dependence of the time instants of complete extinction to the shelf depth and to the processes at the bottom of the permafrost layer and of MHSZ have to be valid irrespective to the applied scenario emission. Further, at long scale, the climate response is determined basically by the cumulative emissions rather than by the pathway details (Zickfeld et al. 2009, 2012). This also provides support that our estimates for timings of the subsea permafrost and the permafrost-associated MHSZ disappearances are correct at least to the order of magnitude.
- We completely lack the centennial-scale climate variability except during the short (few centuries) period with anthropogenic CO_2 emissions. However, this variabilty is likely unimportant for the goals of the present paper owing to (i) this temperature variability is strongly damped near the Arctic shelf floor for the climate of the most part of the Holocene and (ii) large (multi-millennium scale) response times of the subsea permafrost and permafrost-associated MHSZ to external forcing (see Section 1).
- An obvious limitation is due to our selection of the particular Climber-2 grid cell for climate anomalies and the spatially uniform present-day temperature to which these anomalies are added; both are corresponding to the East Siberian Arctic shelf (supplementary Section S3). This is partly reasoned by the major contribution to the permafrost area, MHSZ volume, and MHSZ stock from this part of the Arctic shelf as well as by relatively uniform projections of temperature at these latitudes in Climber-2. In addition, it directly affects only the present-day state rather than future simulations.
- We used hydrostatic pressure to calculate MHSZ boundaries (Section S1). This is similar to Romanovskii et al. (2005); Majorowicz et al. (2012); Hunter et al. (2013); Archer (2015)) and is equivalent to assuming that part of the column remains unfrozen even at very low temperature. However, in some papers (e.g., Tinivella et al. 2019; Liu et al. 2016), alternative pressure calculations, which take into account the lithostatic pressure, are invoked. The latter presumes an existence of completely hydrologically impermeable layers in the sediments and leads to a deeper MHSZ base (Tinivella et al. 2019). The impact of the the replacement of the hydrostatic pressure by a lithostatic one is not explored in our paper.
- We reported the pan-Arctic estimates only for $G = 60\ \mathrm{mW\,m^{-2}}$. This is a typical heat flux from the Earth's interior in the Arctic Ocean (Davies 2013). Arctic shelf regions with substantially larger G lose MHSZ markedly before the emission onset and do not contribute to the estimates. The regions with much smaller geothermal heat flux are untypical for the Arctic shelf.
- At last, there is a caveat in our simulation for ($H_B = 10\,\mathrm{m}$; $G = 45\ \mathrm{mW\,m^{-2}}$) with MHSZ extending down to the bottom of the computation domain boundary and the bottom of the permafrost layer located close to the bottom of the computation domain. This would apparently lead to the misestimated values of all variables under interest. We acknowledge it, and we are going to ameliorate it in future exercises. However, this pair (H_B; G) does not look like 'an outlier' in our simulations, and we believe that the results for this pair are correct at least qualitatively. In addition, the extent of areas with this geothermal heat flux in the Arctic is small (Davies 2013), and all pan-Arctic estimates are done for more common $G = 60\ \mathrm{mW\,m^{-2}}$.
- Our estimate for methane fluxes was constructed assuming an instantaneous transport of methane from MSHZ to the sea floor (Section 2). In reality, this transport is controlled by diffusion and vertical advection. Both pro-

cesses result in a finite timescale for such transport (Xu and Ruppel 2022). Therefore, it is likely that our assumption of an instantaneous transport of methane leads to the overestimated corresponding flux at the sediment-ocean interface.

- We did not model the methane transport through the sediment assuming that there is always a channel transporting up upward. We also tried an alternative the only escaping methane is from the top of the methane hydrate stability zone. Methane produced due to hydrates dissociation at the MHSZ bottom is accumulated below this zone. However, when MHSZ disappears completely, this accumulated methane is instantly transported to the sediment-water interface. Such pulse release is the largest, 125 $\mathrm{gCH_4\,m^{-2}\,yr^{-1}}$, for ($H_B = 50$ m; $G = 75$ $\mathrm{mW\,m^{-2}}$) during 2-5 kyr A.P. (Fig. S7). This value is insensitive to the applied emission scenario. The latter is a consequence of the dominance of the bottom shrinking in the reduction of the MHSZ thickness for this particular case. An order-of-magnitude smaller peak emission as averaged over 2–5 kyr is simulated for $\left(H_B = 50\text{ m};\ G = 60\ \mathrm{mW\,m^{-2}}\right)$, but only in experiment TR3000. Peak CH_4 release per time step is of the same order of magnitude between ($H_B = 50$ m; $G = 75$ $\mathrm{mW\,m^{-2}}$) and $\left(H_B = 50\text{ m};\ G = 60\ \mathrm{mW\,m^{-2}}\right)$ (not shown). In addition, very similar peak release of methane is simulated with the same pairs (H_B; G) irrespective of applied emissions, but at different time instants.
- In addition, we assumed that the hydrate stability zone in our simulations corresponds to pure methane hydrates. A mixture of methane hydrates and hydrates of other species would change the temperature and pressure conditions for the hydrate formation and existence with impacts on time dynamics of such hydrate stability zone. Unaware of the respective conditions, we just mention such a possibility without attempting to quantify it.

Thus, we conclude that our estimates for the time horizons of the subsea permafrost and the permafrost-associated MHSZ are correct at least for the order of magnitude. Moreover, the effects which are neglected in our paper (e.g., the latent heat of hydrates dissociation) may only strenghen our conclusion that their complete disappearance is impossible for at least several kiloyears from the present.

4.4 Final remarks

The simulations with a one-dimensional model for the thermophysics of the sediments for 100 kyr in the future are driven by idealised scenarios of CO_2 emissions and by changes of the parameters of the Earth's orbit.

The most important outcome of our study is as follows:

1. At the outer shelf, permafrost disappears either before the onset of the anthropogenic emissions or during a few centuries after it. In contrast, for the middle and shallow parts of the shelf, in the CO_2-emission forced runs, the subsea permafrost survives, at least, for 5 kyr after the emission onset or even for much longer.
2. At the same parts of the shelf, methane hydrate stability zone (MHSZ) disappears not earlier than at 3 kyr after the CO_2 emission onset.
3. Both permafrost thaw and methane hydrate stability zone shrinking occur mostly from the bottom and depend strongly on the heat flux from the Earth's interior. They are largely independent from the forcing at the upper boundary of the sediments. However, permafrost thaw from the top is basically determined by the applied CO_2 forcing scenario.
4. As a crude estimate, we may state that the CO_2-induced warming in our simulations is able to enhance the pan-Arctic subsea permafrost loss severalfold during 1 kyr after the emissions onset, but it is less important for the respective MHSZ loss.
5. The dynamics of MHSZ is largely independent on the chosen climate projection, at least for the next several thousand years.

One may assume that our study is very idealised and its results are difficult to interpret in terms of common Earth sciences. However, we highlight our general result: the subsea permafrost and the permafrost-associated methane hydrates are unlikely to experience any marked degradation during the next few millennia irrespective (by and large) of the anthropogenic climate forcing. Moreover, most limitations of our model or our setup would only enhance this major conclusion of our paper.

Supplementary Information The online version contains supplementary material available at https://doi.org/10.1007/s00704-023-04804-7.

Acknowledgements The authors are grateful to A. Ganopolski for making the Climber-2 output available.

Author contribution V.V.M.: conceptualisation, model simulations, manuscript preparation, and editing. A.V.E.: conceptualisation, manuscript preparation, and editing.

Funding Estimates of the timescales of the subsea permafrost and the permafrost-associated methane hydrates response to external forcing are supported by the Russian Science Foundation grant 23-47-00104. The development of the model for the subsea sediments thermodynamics is supported by the Ministry of Education and Science of the

Russian Federation (NIOKTR 123081400010-2, the agreement no. 075-03-2023-506/1)

Availability of data and materials The SMILES simulations output used in this paper is available at the ZENODO repository via https://doi.org/10.5281/zenodo.5728529.

Code availility The SMILES code is available from the first author by request.

Declarations

Ethics approval Not applicable

Consent to participate Not applicable

Consent for publication Not applicable

Conflict of interest The authors declare no competing interests.

References

Alekseev D, Koshurnikov A, Gunar A et al (2023) Time-domain electromagnetics for subsea permafrost mapping in the Arctic: the synthetic response analyses and uncertainty estimates from numerical modelling data. Geosciences 13(5):144. https://doi.org/10.3390/geosciences13050144

Angelopoulos M, Overduin P, Miesner F et al (2020) Recent advances in the study of Arctic submarine permafrost. Permafrost Perigl Proc 31(3):442–453. https://doi.org/10.1002/ppp.2061

Angelopoulos M, Overduin P, Jenrich M et al. (2021) Onshore thermokarst primes subsea permafrost degradation. Geophys Res Lett 48(20):e2021GL093,881. https://doi.org/10.1029/2021GL093881

Anisimov O, Borzenkova I, Lavrov S et al (2012) The current dynamics of the submarine permafrost and methane emissions on the shelf of the Eastern Arctic seas. Ice Snow 52(2):97–105 ([in Russian])

Archer D (2007) Methane hydrate stability and anthropogenic climate change. Biogeosciences 4(4):521–544

Archer D (2015) A model of the methane cycle, permafrost, and hydrology of the Siberian continental margin. Biogeosciences 12(10):2953–2974. https://doi.org/10.5194/bg-12-2953-2015

Archer D, Ganopolski A (2005) A movable trigger: fossil fuel CO_2 and the onset of the next glaciation. Geochem Geophys Geosyst 6(5):Q05,003. https://doi.org/10.1029/2004GC000891

Arzhanov M, Malakhova V (2023) Modeling the accumulation and transition to the relic state of methane hydrates in the permafrost of northwestern Siberia. Izvestiya, Phys Soild Earth 59(2):242–253. https://doi.org/10.1134/S1069351323020040

Berchet A, Bousquet P, Pison I et al (2016) Atmospheric constraints on the methane emissions from the East Siberian Shelf. Atmos Chem Phys 16(6):4147–4157. https://doi.org/10.5194/acp-16-4147-2016

Biastoch A, Treude T, Rüpke L et al. (2011) Rising Arctic Ocean temperatures cause gas hydrate destabilization and ocean acidification. Geophys Res Lett 38(8):L08,602. https://doi.org/10.1029/2011GL047222

Bogoyavlensky V, Kishankov A, Yanchevskaya A et al (2018) Forecast of gas hydrates distribution zones in the Arctic Ocean and adjacent offshore areas. Geosciences 8(12):453. https://doi.org/10.3390/geosciences8120453

Bogoyavlensky V, Kishankov A, Kazanin A et al (2022) Distribution of permafrost and gas hydrates in relation to intensive gas emission in the central part of the Laptev Sea (Russian Arctic). Mar Petrol Geol 138(105):527. https://doi.org/10.1016/j.marpetgeo.2022.105527

Bogoyavlensky V, Kishankov A, Kazanin A (2023) Evidence of large-scale absence of frozen ground and gas hydrates in the northern part of the East Siberian Arctic shelf (Laptev and East Siberian seas). Mar Petrol Geol 148(106):050. https://doi.org/10.1016/j.marpetgeo.2022.106050

Boswell R, Rose K, Collett T et al (2011) Geologic controls on gas hydrate occurrence in the Mount Elbert prospect. Alaska North Slope. Mar Petrol Geol 28(2):589–607. https://doi.org/10.1016/j.marpetgeo.2009.12.004

Buffett B (2000) Clathrate hydrates. Annu Rev Earth Planet Sci 28:477–507. https://doi.org/10.1146/annurev.earth.28.1.477

Buffett B, Archer D (2004) Global inventory of methane clathrate: sensitivity to changes in the deep ocean. Earth Planet Sci Lett 227(3–4):185–199. https://doi.org/10.1016/j.epsl.2004.09.005

Bukhanov B, Chuvilin E, Zhmaev M et al. (2023) In situ bottom sediment temperatures in the Siberian Arctic seas: current state of subsea permafrost in the Kara sea vs Laptev and East Siberian seas. Mar Petrol Geol 157:106,467. https://doi.org/10.1016/j.marpetgeo.2023.106467

Canadell J, Monteiro P, Costa M et al. (2021) Global carbon and other biogeochemical cycles and feedbacks. In: Masson-Delmotte V, Zhai P, Pirani A, et al (eds) Climate Change 2021: The Physical Science Basis. Contribution of Working Group I to the Sixth Assessment Report of the Intergovernmental Panel on Climate Change. Cambridge University Press, Cambridge and New York, pp 673–815

Chuvilin E, Bukhanov B, Davletshina D et al (2018) Dissociation and self-preservation of gas hydrates in permafrost. Geosciences 8(12):431. https://doi.org/10.3390/geosciences8120431

Chuvilin E, Bukhanov B, Yurchenko A et al (2022) In-situ temperatures and thermal properties of the East Siberian Arctic shelf sediments: key input for understanding the dynamics of subsea permafrost. Mar Petrol Geol 138(105):550. https://doi.org/10.1016/j.marpetgeo.2022.105550

Davies J (2013) Global map of solid Earth surface heat flow. Geochem Geophys Geosyst 14(10):4608–4622. https://doi.org/10.1002/ggge.20271

Dean J, Middelburg J, Röckmann T et al (2018) Methane feedbacks to the global climate system in a warmer world. Rev Geophys 56(1):207–250. https://doi.org/10.1002/2017RG000559

Denisov S, Arzhanov M, Eliseev A et al (2011) Assessment of the response of subaqueous methane hydrate deposits to possible climate change in the twenty first century. Doklady Earth Sci 441(2):1706–1709. https://doi.org/10.1134/S1028334X11120129

Dickens G, O'Neil J, Rea D et al (1995) Dissociation of oceanic methane hydrate as a cause of the carbon isotope excursion at the end of the Paleocene. Paleoceanography 10(6):965–971. https://doi.org/10.1029/95PA02087

Dmitrenko I, Kirillov S, Tremblay L et al. (2011) Recent changes in shelf hydrography in the Siberian Arctic: potential for subsea permafrost instability. J Geophys Res: Oceans 116(C10):C10,027. https://doi.org/10.1029/2011JC007218

Eliseev A, Malakhova V, Arzhanov M et al (2015) Changes in the boundaries of the permafrost layer and the methane hydrate stability zone on the Eurasian Arctic Shelf, 1950–2100. Doklady Earth Sci 465(2):1283–1288. https://doi.org/10.1134/S1028334X15120107

Eyring V, Bony S, Meehl G et al (2016) Overview of the coupled model intercomparison project phase 6 (CMIP6) experimental design and organization. Geosci Model Dev 9(5):1937–1958. https://doi.org/10.5194/gmd-9-1937-2016

Fox-Kemper B, Hewitt H, Xiao C et al. (2021) Ocean, cryosphere and sea level change. In: Masson-Delmotte V, Zhai P, Pirani A, et al (eds) Climate Change 2021: The Physical Science Basis. Contribution of Working Group I to the Sixth Assessment Report of the Intergovernmental Panel on Climate Change. Cambridge University Press, Cambridge and New York, pp 1211–1361

Frederick J, Buffett B (2014) Taliks in relict submarine permafrost and methane hydrate deposits: pathways for gas escape under present and future conditions. J Geophys Res: Earth Surface 119(2):106–122. https://doi.org/10.1002/2013JF002987

Friedlingstein P, O'Sullivan M, Jones M et al (2020) Global Carbon Budget 2020. Earth Syst Sci Data 12(4):3269–3340. https://doi.org/10.5194/essd-12-3269-2020

Ganopolski A, Winkelmann R, Schellnhuber H (2016) Critical insolation-CO_2 relation for diagnosing past and future glacial inception. Nature 529(7585):200–203. https://doi.org/10.1038/nature16494

Gavrilov A, Malakhova V, Pizhankova E et al (2020) Permafrost and gas hydrate stability zone of the glacial part of the East-Siberian shelf. Geosciences 10(12):484. https://doi.org/10.3390/geosciences10120484

Gavrilov A, Pavlov V, Fridenberg A et al (2020) The current state and 125 kyr history of permafrost on the Kara Sea shelf: modeling constraints. Cryosphere 14(6):1857–1873. https://doi.org/10.5194/tc-14-1857-2020

Golubeva E, Platov G, Malakhova V et al (2018) Modelling the long-term and inter-annual variability in the Laptev Sea hydrography and subsea permafrost state. Polarforschung 87(2):195–210. https://doi.org/10.2312/polarforschung.87.2.195

Gornitz V, Fung I (1994) Potential distribution of methane hydrates in the world's oceans. Glob Biogeochem Cycles 8(3):335–347. https://doi.org/10.1029/94GB00766

Heuzé C, Heywood K, Stevens D et al (2015) Changes in global ocean bottom properties and volume transports in CMIP5 models under climate change scenarios. J Climate 28(8):2917–2944. https://doi.org/10.1175/JCLI-D-14-00381.1

Hunter S, Goldobin D, Haywood A et al (2013) Sensitivity of the global submarine hydrate inventory to scenarios of future climate change. Earth Planet Sci Lett 367:105–115. https://doi.org/10.1016/j.epsl.2013.02.017

Ivanov V (2023) Arctic sea ice loss enhances the oceanic contribution to climate change. Atmosphere 14(2):409. https://doi.org/10.3390/atmos14020409

James R, Bousquet P, Bussmann I et al (2016) Effects of climate change on methane emissions from seafloor sediments in the Arctic Ocean: a review. Limnol Oceanogr 61(51):S283–S299. https://doi.org/10.1002/lno.10307

Klauda J, Sandler S (2005) Global distribution of methane hydrate in ocean sediment. Energy Fuels 19(2):459–470. https://doi.org/10.1021/ef049798o

Koshurnikov A (2023) Permafrost of the Russian Arctic Seas shelf (according to geophysical studies). Lomonosov Moscow State University, Moscow (**[in Russian]**)

Lamarque JF (2008) Estimating the potential for methane clathrate instability in the 1%-CO2 IPCC AR-4 simulations. Geophys Res Lett 35(19):L19,806. https://doi.org/10.1029/2008GL035291

Lique C, Johnson H, Plancherel Y (2018) Emergence of deep convection in the Arctic Ocean under a warming climate. Clim Dyn 50(9):3833–3847. https://doi.org/10.1007/s00382-017-3849-9

Liu S, Jiang Z, Liu H et al (2016) The natural-gas hydrate exploration prospects of the Nayixiong Formation in the Kaixinling-Wuli Permafrost, Qinghai-Tibet Plateau. Mar Petrol Geol 72:179–192. https://doi.org/10.1016/j.marpetgeo.2016.01.022

MacDonald G (1990) Role of methane clathrates in past and future climates. Clim Change 16(3):247–281. https://doi.org/10.1007/BF00144504

MacDougall A, Frölicher T, Jones C et al (2020) Is there warming in the pipeline? A multi-model analysis of the zero emissions commitment from CO_2. Biogeosciences 17(11):2987–3016. https://doi.org/10.5194/bg-17-2987-2020

Majorowicz J, Safanda J, Osadetz K (2012) Inferred gas hydrate and permafrost stability history models linked to climate change in the Beaufort-Mackenzie Basin. Arctic Canada. Climate of the Past 8(2):667–682. https://doi.org/10.5194/cp-8-667-2012

Majorowicz J, Osadetz K, Safanda J (2015) Models of talik, permafrost and gas hydrate histories - Beaufort Mackenzie Basin. Canada. Energies 8(7):6738–6764. https://doi.org/10.3390/en8076738

Majumdar U, Cook A (2018) The volume of gas hydrate-bound gas in the northern Gulf of Mexico. Geochem Geophys Geosyst 19(11):4313–4328. https://doi.org/10.1029/2018GC007865

Malakhova V (2020) The response of the Arctic Ocean gas hydrate associated with subsea permafrost to natural and anthropogenic climate changes. IOP Conf Ser: Earth and Environl Sci 606(012):035. https://doi.org/10.1088/1755-1315/606/1/012035

Malakhova V, Eliseev A (2017) The role of heat transfer time scale in the evolution of the subsea permafrost and associated methane hydrates stability zone during glacial cycles. Glob Planet Change 157:18–25. https://doi.org/10.1016/j.gloplacha.2017.08.007

Malakhova V, Eliseev A (2018) Influence of rift zones and thermokarst lakes on the formation of subaqueous permafrost and the stability zone of methane hydrates of the Laptev Sea shelf in the Pleistocene. Ice and Snow 58(2):231–242. https://doi.org/10.15356/2076-6734-2018-2-231-242, [in Russian]

Malakhova V, Eliseev A (2020a) Salt diffusion effect on the submarine permafrost state and distribution as well as the stability zone of methane hydrates on the Laptev Sea shelf. Ice and Snow 60(4):533–546. https://doi.org/10.31857/S2076673420040058, [in Russian]

Malakhova V, Eliseev A (2020) Uncertainty in temperature and sea level datasets for the Pleistocene glacial cycles: implications for thermal state of the subsea sediments. Glob Planet Change 192(103):249. https://doi.org/10.1016/j.gloplacha.2020.103249

Malakhova V, Eliseev A (2023) A relationship between changes of surface air and sea floor temperatures at the arctic shelf from the coupled models intercomparison project, phase 6 data. Atmosphere 14(6):1024. https://doi.org/10.3390/atmos14061024

Malakhova V, Golubeva E (2016) Estimation of the permafrost stability on the East Arctic shelf under the extreme climate warming scenario for the XXI century. Ice and Snow 56(1):61–72. https://doi.org/10.15356/2076-6734-2016-1, [in Russian]

Malakhova V, Golubeva E (2022) Model study of the effects of climate change on the methane emissions on the Arctic Shelves. Atmosphere 13(2):274. https://doi.org/10.3390/atmos13020274

Matveeva T, Kaminsky V, Semenova A et al (2020) Factors affecting the formation and evolution of permafrost and stability zone of gas hydrates: case study of the Laptev Sea. Geosciences 10(12):504. https://doi.org/10.3390/geosciences10120504

McGuire A, Anderson L, Christensen T et al (2009) Sensitivity of the carbon cycle in the Arctic to climate change. Ecol Monographs 79(4):523–555. https://doi.org/10.1890/08-2025.1

Mestdagh T, Poort J, De Batist M (2017) The sensitivity of gas hydrate reservoirs to climate change: perspectives from a new combined model for permafrost-related and marine settings. Earth Sci Rev 169:104–131. https://doi.org/10.1016/j.earscirev.2017.04.013

Notz D, SIMIP Community (2020) Arctic sea ice in CMIP6. Geophys Res Lett 47(10):e2019GL086,749. https://doi.org/10.1029/2019GL086749

O'Connor F, Boucher O, Gedney N et al. (2010) Possible role of wetlands, permafrost, and methane hydrates in the methane cycle under future climate change: a review. Rev Geophys 48(4):RG4005. https://doi.org/10.1029/2010RG000326

Overduin P, Schneider von Deimling T, Miesner F et al (2019) Submarine permafrost map in the arctic modeled using 1-D transient heat flux (SuPerMAP). J Geophys Res: Oceans 124(6):3490–3507. https://doi.org/10.1029/2018JC014675

Pollack H, Hurter S, Johnson J (1993) Heat flow from the Earth's interior: analysis of the global data set. Rev Geophys 31(3):267–280. https://doi.org/10.1029/93RG01249

Portnov A, Mienert J, Serov P (2014) Modeling the evolution of climate-sensitive Arctic subsea permafrost in regions of extensive gas expulsion at the West Yamal shelf. J Geophys Res: Biogeosciences 119(11):2082–2094. https://doi.org/10.1002/2014JG002685

Razumov S, Spektor V, Grigoriev M (2014) Model of the post-Cenozoic evolution of the cryolithozone of the shelf of the western part of the Laptev Sea. Oceanology 54(5):637–649. https://doi.org/10.1134/S0001437014040092

Reagan M, Moridis G (2008) Dynamic response of oceanic hydrate deposits to ocean temperature change. J Geophys Res: Oceans 113(C12):C12,023. https://doi.org/10.1029/2008JC004938

Reagan M, Moridis G, Elliott S et al. (2011) Contribution of oceanic gas hydrate dissociation to the formation of Arctic Ocean methane plumes. J Geophys Res: Oceans 116(C9):C09,014. https://doi.org/10.1029/2011JC007189

Romanovskii N, Hubberten HW, Gavrilov A et al (2005) Offshore permafrost and gas hydrate stability zone on the shelf of East Siberian Seas. Geo-Mar Lett 25(2–3):167–182. https://doi.org/10.1007/s00367-004-0198-6

Romanovskii N, Eliseeva A, Gavrilov A et al. (2006) The long-term dynamics of the permafrost and gas hydrate stability zone on rifts of the East Siberian Arctic shelf (report 2). Earth Cryosphere X(1):29–38

Ruppel C, Kessler J (2017) The interaction of climate change and methane hydrates. Rev Geophys 55(1):126–168. https://doi.org/10.1002/2016RG000534

Ruppel C, Waite W (2020) Timescales and processes of methane hydrate formation and breakdown, with application to geologic systems. J Geophys Res: Solid Earth 125(8):e2018JB016,459. https://doi.org/10.1029/2018JB016459

Sapart C, Shakhova N, Semiletov I et al (2017) The origin of methane in the East Siberian Arctic Shelf unraveled with triple isotope analysis. Biogeosciences 14(9):2283–2292. https://doi.org/10.5194/bg-14-2283-2017

Saunois M, Stavert A, Poulter B et al (2020) The global methane budget 2000–2017. Earth Syst Sci Data 12(3):1561–1623. https://doi.org/10.5194/essd-12-1561-2020

Shakhova N, Semiletov I, Salyuk A et al (2010) Extensive methane venting to the atmosphere from sediments of the East Siberian Arctic Shelf. Science 327(5970):1246–1250. https://doi.org/10.1126/science.1182221

Shakhova N, Semiletov I, Chuvilin E (2019) Understanding the permafrost-hydrate system and associated methane releases in the East Siberian Arctic Shelf. Geosciences 9(6):251. https://doi.org/10.3390/geosciences9060251

Stranne C, O'Regan M, Jakobsson M (2016) Overestimating climate warming-induced methane gas escape from the seafloor by neglecting multiphase flow dynamics. Geophys Res Lett 43(16):8703–8712. https://doi.org/10.1002/2016GL070049

Stranne C, O'Regan M, Dickens G et al (2017) Dynamic simulations of potential methane release from East Siberian continental slope sediments. Geochem Geophys Geosyst 17(3):872–886. https://doi.org/10.1002/2015GC006119

Tinivella U, Giustiniani M, Marin-Moreno H (2019) A quick-look method for initial evaluation of gas hydrate stability below subaqueous permafrost. Geosciences 9(8):329. https://doi.org/10.3390/geosciences9080329

Wilkenskjeld S, Miesner F, Overduin P et al (2021) Strong increase of thawing of subsea permafrost in the 22nd century caused by anthropogenic climate change. Cryosphere Discussions 2021:1–18. https://doi.org/10.5194/tc-2021-231

Xu W, Ruppel C (2022) Predicting the occurrence, distribution, and evolution of methane gas hydrate in porous marine sediments. J Geophys Res: Solid Earth 104(B3):5081–5095. https://doi.org/10.1029/1998JB900092

Yang D, Marsh P, Ge S (2014) Heat flux calculations for Mackenzie and Yukon rivers. Polar Sci 8(3):232–241. https://doi.org/10.1016/j.polar.2014.05.001

Zeebe R (2012) History of seawater carbonate chemistry, atmospheric CO_2, and ocean acidification. Annu Rev Earth Planet Sci 40:141–165. https://doi.org/10.1146/annurev-earth-042711-105521

Zickfeld K, Eby M, Matthews H et al. (2009) Setting cumulative emissions targets to reduce the risk of dangerous climate change. Proc Nat Acad Sci 106(38):16,129–16,134. https://doi.org/10.1073/pnas.0805800106

Zickfeld K, Arora V, Gillett N (2012) Is the climate response to CO_2 emissions path dependent? Geophys Res Lett 39(5):L05,703. https://doi.org/10.1029/2011GL050205

Supplementary information to *Subsea permafrost and associated methane hydrate stability zone: how long will they survive in the future?*

Valentina V. Malakhova and Alexey V. Eliseev

S1 SMILES description

Our model, SMILES (the Sediment Model Invented for Long-tErm Simulations) solves the one–dimensional equation for heat diffusion in the sediments

$$C\frac{\partial T}{\partial t} = \frac{\partial}{\partial z}\left(\kappa\frac{\partial T}{\partial z}\right) \tag{S1}$$

as well as the diffusion equation for salinity

$$\frac{\partial\left(WS\right)}{\partial t} = \frac{\partial}{\partial z}\left(D_S\frac{\partial S}{\partial t}\right). \tag{S2}$$

Here C is heat capacity per unit volume, T is temperature, t is time, z is vertical coordinate below the sediment top (positive downward), κ is thermal conductivity, W is volumetric moisture content of the sediment, S is salinity, and D_S is salt diffusivity. We set C and κ as it is figured in Table S1. These values are in agreement with those measured by Chuvilin et al (2021, 2022) as well with those selected by Matveeva et al (2020). Salt diffusivity in the unfrozen layers is $D_S = 10^{-9}\,\mathrm{m}^2\,\mathrm{s}^{-1}$, and it is zeroed if layer is frozen. The latter values were derived in (Razumov et al, 2014) from the oceanic sediment drilling measurements.

Boundaries $z = z_\mathrm{F}$ between the frozen and unfrozen sediment layers are determined by temperature condition

$$T\big|_{z_\mathrm{F}} = T_\mathrm{F}, \tag{S3}$$

At these boundaries, the Stefan condition is imposed:

$$\kappa_\mathrm{u}\left.\frac{\partial T}{\partial z}\right|_\mathrm{u} - \kappa_\mathrm{f}\left.\frac{\partial T}{\partial z}\right|_\mathrm{f} = \mathcal{L}W\frac{\partial z_\mathrm{F}}{\partial t}. \tag{S4}$$

where $\mathcal{L}$ is latent heat of fusion, and W is volumetric moisture content of the sediment, subscripts 'u' and 'f' depict values of the thermal properties corresponding to unfrozen and frozen layers correspondingly. Volumetric latent

Table S1: Thermophysical properties of the sediments: heat capacity C and heat diffusivity κ as prescribed in the sediments.

z, m	lithology	dry soil density, kg m^{-3}	porosity, %	C, $\mathrm{MJ\,m^{-3}\,K^{-1}}$		κ, $\mathrm{W\,m^{-1}\,K^{-1}}$	
				unfrozen	frozen	unfrozen	frozen
0-200	sand, loam	1500	20-40	2.63	2.01	1.38	2.30
200-800	sandy loam, clay	1800	12-20	2.70	2.34	1.75	2.70
800-1500	sandstone, mudstone	2000	1-12	2.15	2.10	2.30	2.75

heat of fusion is set equal to the value corresponding to the distilled water, $3.34 \times 10^8\,\mathrm{J\,m^{-3}}$.

Heat and salt diffusion equations are coupled via T_F dependence on S and pressure P (Galushkin et al, 2012):

$$T_\mathrm{F} = -\alpha_P P - \alpha_S S \tag{S5}$$

with $\alpha_P = 7.3\times10^{-2}\,\mathrm{MPa^{-1}}$ and $\alpha_S = 6.4\times10^{-2}\,\mathrm{psu^{-1}}$ (psu is practical salinity unit).

The boundary conditions for Eqs. (S1) and (S2) at the top of the sediments are

$$T|_{z=0} = T_\mathrm{B} \tag{S6}$$

and

$$S|_{z=0} = S_\mathrm{B}. \tag{S7}$$

The respective boundary conditions at the bottom of the computational domain in the sediments

$$\kappa \frac{\partial T}{\partial z}\bigg|_{z=H_\mathrm{S}} = G \tag{S8}$$

and

$$S|_{z=H_\mathrm{S}} = 0. \tag{S9}$$

Here H_S is thickness of the computational domain in the sediment column. We set $H_\mathrm{S} = 1,500\,\mathrm{m}$.

We assume that sediment pores are filled with water up to their holding capacity. Sediment porosity exponentially decreases downward from the value 0.4 at the top of the sediments with the vertical scale 2,500 m (Sclater and Christie, 1980). The same porosity dependence on depth is used by Matveeva et al (2020).

Model equations are solved by using the sweep method at a discrete vertical grid with a vertical step of 0.5 m. Time stepping scheme is implicit with the a time step of 1 mo. We do not resolve annual cycle.

The equilibrium pressure–temperature curve for methane hydrates is adopted from the TOUGH$^+$HYDRATE model as it is reported in the inlet to Fig. 1 of (Reagan and Moridis, 2008):

$$\ln\left(P_\mathrm{h}\right) = \sum_{n=0}^{5} a_n T_\star^n, \tag{S10}$$

with a_n as figured in Table S2. Here $T_\star$ is temperature corrected to the salt-induced depression

$$T_\star = T - \Delta T_\mathrm{d} \tag{S11}$$

with

$$\Delta T_\mathrm{d} = \Delta T_\mathrm{d,ref} \frac{\ln\left(1 - x_\mathrm{s}\right)}{\ln\left(1 - x_\mathrm{s,ref}\right)}. \tag{S12}$$

Here x_s is molar fraction of salt in the pore water, $\Delta T_\mathrm{D,ref} = 2\,\mathrm{K}$, $x_\mathrm{s,ref} = 0.0134$ (Reagan et al, 2011).

Table S2: Coefficients a_n in Eq. (S10). Temperature $T_\star$ is in kelvins and the equilibrium pressure P_h is in megapascals.

n	$T_\star > 273.2\,\mathrm{K}$	$T_\star < 273.2\,\mathrm{K}$
0	-1.94138504464560	-4.38921173434628
1	3.31018213397926	7.76302133739303
2	-2.25540264493806	-7.27291427030502
3	+7.67559117787059	3.85413985900724
4	-1.30465829788791	-1.03669656828834
5	8.86065316687571	1.09882180475307

S2 Initial conditions

Initial temperature distribution (Fig. S5a) is prescribed as

$$T(z_j, t = 0) = T(z_{j-1}, t = 0) + G\,(z_j - z_{j-1})\,/\kappa_j.$$

Here subscript j indicates computational level within the sediment (numbered from top to bottom), κ_j is thermal conductivity at this level, and $T(z_0, t = 0) = T_\mathrm{B}(t = 0)$. The resulting $T(z, t = 0)$ is almost linear with respect to z. Such profile would be in equilibrium with the specified boundary conditions provided that heat diffusivity is independent from the vertical coordinate. However, because heat diffusivity changes in the vertical direction between frozen and unfrozen layers, we need to spin up the model for 3 kyr.

Initial condition for salt diffusion equation is prescribed as a final state from the previous run (Malakhova and Eliseev, 2020) to avoid strong salinity drift. Namely, the glaciation cycle for 400-340 kyr B.P. (before present) is repeated several times, and S drift is visually inspected in the whole computational column. It appeared that 7 repetitions of this cycle is enough to achieve the salinity drift throughout the whole computational domain. Then, the final output of this spin up was used for the non-glacial conditions 400 kyr B.P.

S3 Boundary conditions

At the sediment–ocean interface (or at the sediment–air interface if the sediments are in contact with the air during oceanic regressions), temperature and salinity are prescribed to time-dependent functions T_B and S_B. In particular, when shelf is in contact with the atmosphere, T_B is set equal to air temperature T_a, and S_B is zeroed. When shelf is covered by water, T_B (S_B) is prescribed to be equal to the near–bottom water temperature (salinity) T_w (S_w). Both T_w and S_w are functions of the present-day shelf depth H_B (Table S3) and include the offsets between the near-surface air temperature and the temperature at the sea floor (thus, $T_\mathrm{B} \neq T_\mathrm{a}$ when the shelf is flooded). In addition to this at the time of the post-glacial oceanic transgression, we calculate the fraction of

Table S3: T_w and S_w as functions of the present-day shelf depth H_B.

H_B, m	T_w, °C	S_w, psu
10	-1.3	27
50	-1.7	34
100	-1.9	34

time when water layer thickness is smaller than $z_\star = 0.5\,\mathrm{m}$. This fraction is computed as $(z_\star/10\,\mathrm{m}) \times t_{10}$, and t_{10} is the time interval to rise the sea level from $-10\,\mathrm{m}$ to zero. For this time interval, it is assumed that $T_\mathrm{w} = -0.5^o\mathrm{C}$ and $S_\mathrm{w} = 25\,\mathrm{psu}$. At the bottom of sediment domain (1,500 m in our model), time-independent heat flux G from the Earth interior and no-flux condition for salinity are adapted.

Time-dependent T_a is constructed from the monthly mean SAT as simulated with the CLIMBER-2 for time interval from 400 kyr B.P. to the time instant $t = 0$, which corresponds to the common era (C.E.) year 1950 (Ganopolski et al, 2016). The resulting T_B is shown in Fig. S1.

From the CLIMBER-2 output, a grid cell, which covers the East Siberian Arctic shelf (ESAS), is extracted. Note that because of very coarse horizontal resolution of CLIMBER-2 (10^o in latitude and 51.4^o in longitude; Petoukhov et al, 2000), a single grid cell covers the entire EEAS (the area from 77.1^oE to 128.6^oE and from 70^oN to 80^oN). CLIMBER-2 output is available as anomalies from the above-defined present-day state. Thus, T_a is constructed by adding the present-day temperature in this area (-12^oC, Nicolsky et al, 2012) to the CLIMBER-2 output (Fig S2).

Then, our simulations are continued for 100 kyr ('future'; $t > 0$). For future, we assume that the shelf is always covered by the water, but SAT changes. Thus, for future $T_\mathrm{B} = T_\mathrm{w} + \Delta T_\mathrm{fut}$. In the first series of simulations, ΔT_fut is set equal to $T_\mathrm{a}(t) - T_\mathrm{a}(0)$. For this, we use the continuation of the CLIMBER-2 simulations forced by changes of parameters of the Earth orbit and by anthropogenic CO_2 emissions into the atmosphere (Ganopolski et al, 2016). These emissions start in nominal year 1950 and proceed with the same, simulation- and time-independent rate until the prechosen cumulative emission level E_tot is achieved. Upon this, anthropogenic CO_2 emission rate is set to zero, and the CLIMBER-2 simulation is continued with a freely evolving carbon cycle.

The SMILES simulation employing T_B, which is based on the CLIMBER-2 simulation with $E_\mathrm{tot} = 1000\,\mathrm{PgC}$, is denoted as TR1000. In a similar fashion, we use the CLIMBER-2 output for the simulation with $E_\mathrm{tot} = 3000\,\mathrm{PgC}$ to construct the forcing for our simulation further denoted TR3000. In turn, our simulation TR0 is forced by T_a, which is a repetition of the CLIMBER-simulated SAT for year 1950 C.E. copied for the whole future period (thus, $\Delta T_\mathrm{fut} \equiv 0$ in TR0).

The CLIMBER-simulated SAT anomalies in the above-mentioned grid cell differ from the zonal mean SAT change at the same latitude no more than by 20%

for the entire TR3000 simulation. For the TR1000 simulation, the respective difference is within 10% except for the period 55-60 kyr in future and for the last 10 kyr of the simulation (Fig. S4).

We neglect the impact of future sea level rise on hydrostatic pressure.

Depending on simulation, G is set equal to either $45\,\mathrm{mW\,m^{-2}}$ or to $60\,\mathrm{mW\,m^{-2}}$ or to $75\,\mathrm{mW\,m^{-2}}$.

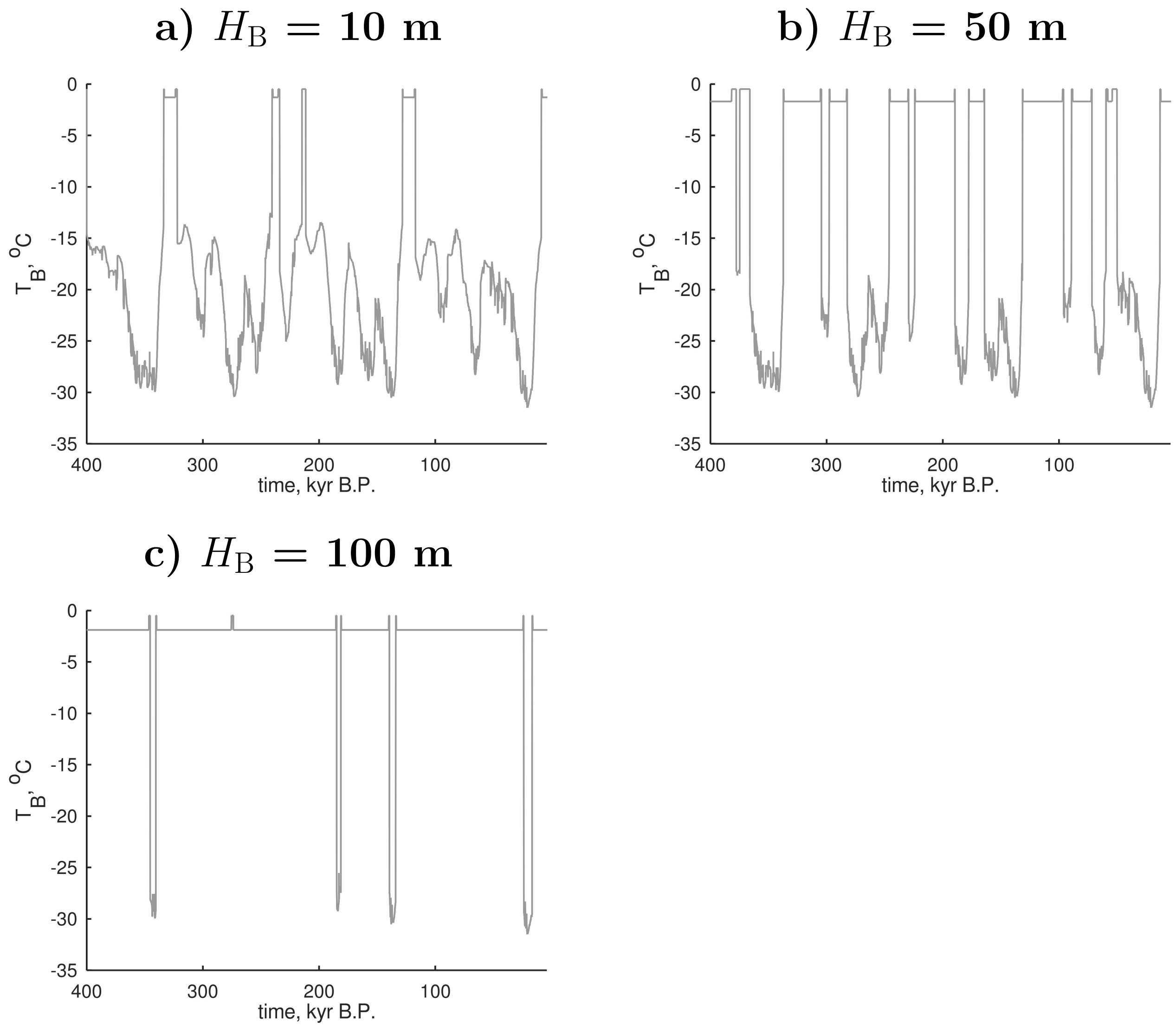
a) H_B = 10 m

b) H_B = 50 m

c) H_B = 100 m

Figure S1: Past temperature at the sediment top for different present-day shelf depths H_B.

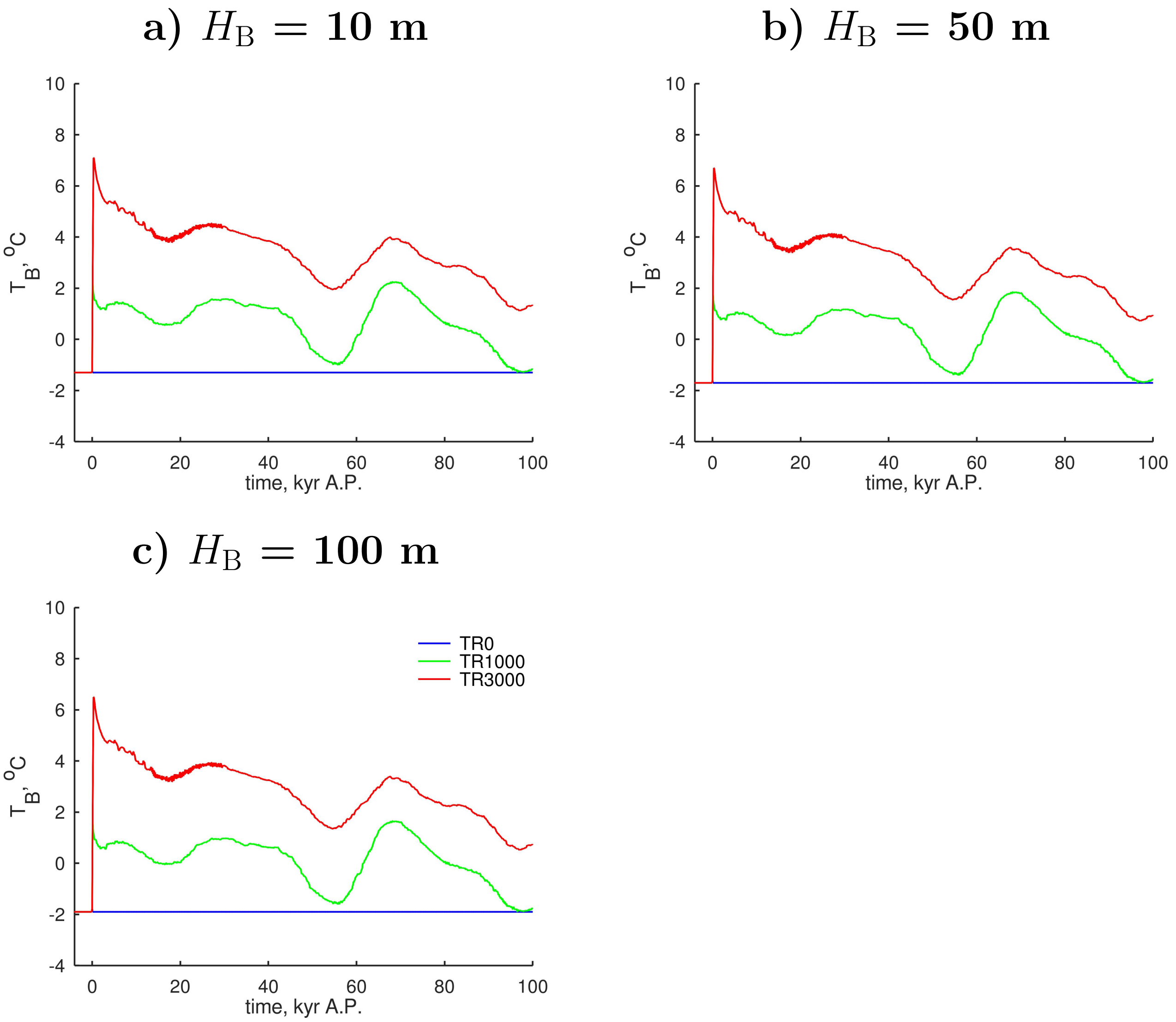

Figure S2: Future temperature at the sediment top for different present-day shelf depths H_B.

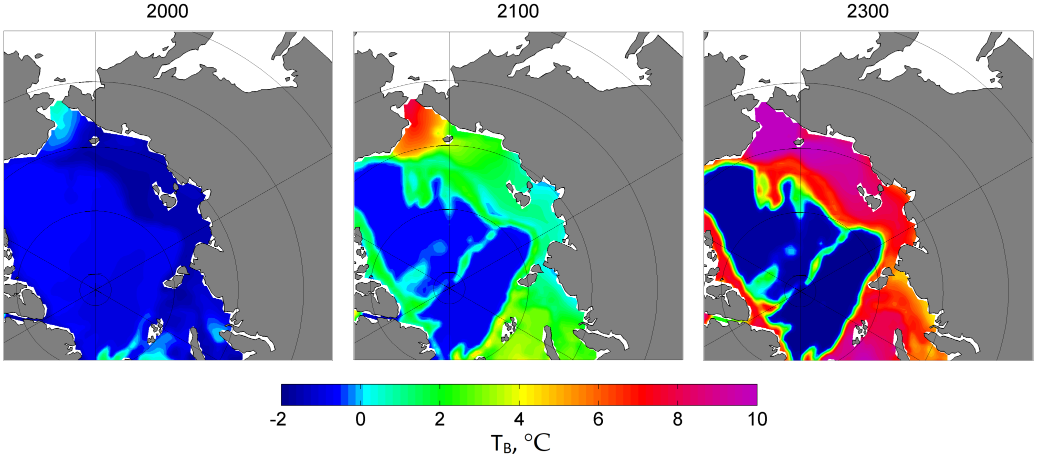

Figure S3: The seafloor temperature (degrees Centigrade) in the simulation with Earth system model ACCESS ESM-1.5 forced by the Shared Socioeconomic Pathways (SSP) 5-8.5 scenario. The data for this plot were downloaded from the https://esgf-node.llnl.gov/projects/cmip6/ homesite (last access June, 07, 2022).

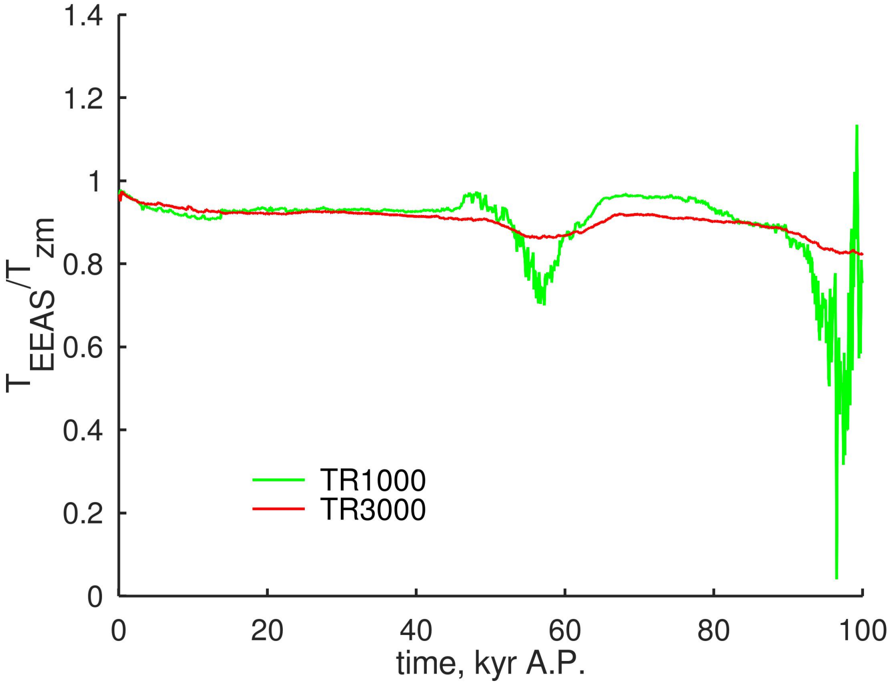

Figure S4: Ratio of the CLIMBER-simulated surface air temperature anomalies in the selected grid cell to zonal mean at the same latitude

S4 Additional results

S4.1 Temperature and salinity in the sediments at $t = 0$

.

Temperature and salinity profiles in the sediments at $t = 0$ are shown in Fig. S5.

Temperature at the time instant is below the freezing threshold for all H_{B} and increases downward with a H_{B}-depending slope.

After the model spin up salinity is close to the typical sea water values (around 30‰) near the sea floor (Fig S5b). In the shallow and intermediate parts of the shelf, salinity drops within few tens of meters. In the shallow shelf, it is about 20‰) at the depth 10 m below the sea floor, and below the depth of 30 m relative to the sea floor, S amounts to few per mil. In the intermediate shelf salinity value 10‰ is reached at the corresponding depth 50 m relative to the sea floor. In the outer shelf, S is markedly larger and, as a whole, is above 15‰ until the depth 100 m below the sea floor.

a) $T\,(t = 0)$

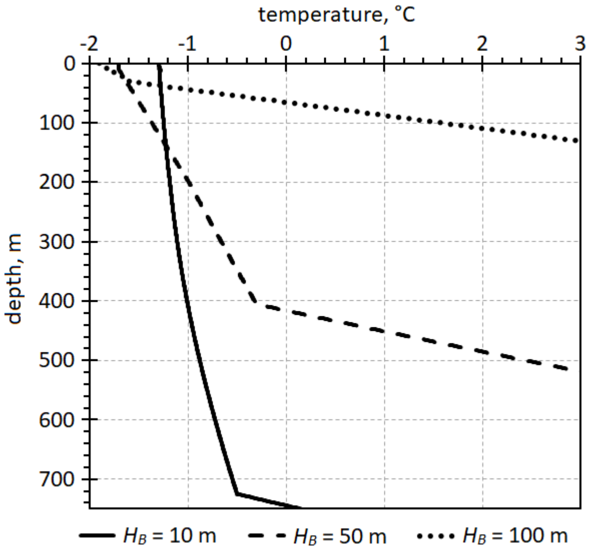

b) $S\,(t = 0)$

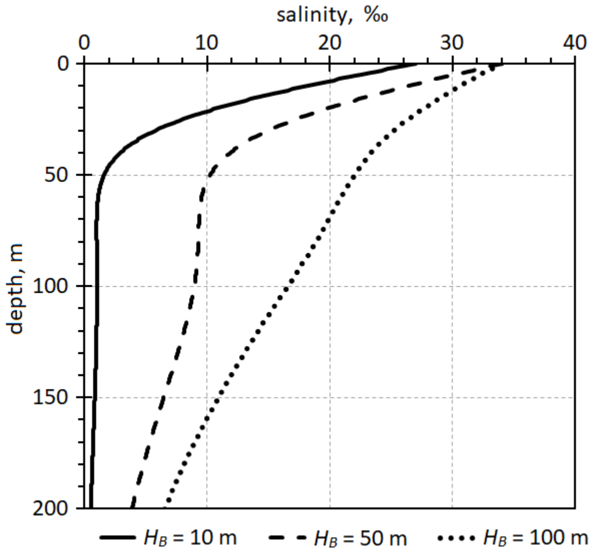

Figure S5: Profiles of temperature (a) and salinity (b) at $t = 0$ for different present-day shelf depths H_{B}. Note different Y-axes range between panels a and b.

S4.2 Simulation results for $t \leq 0$

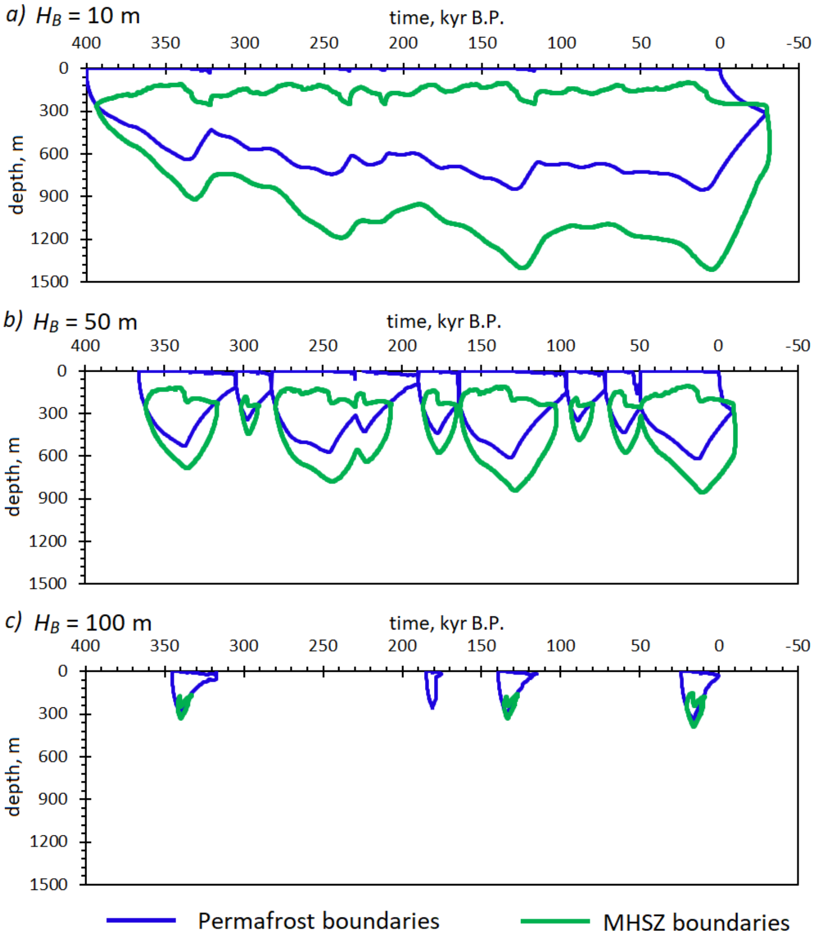

Figure S6: The permafrost and MHSZ boundaries in the simulation TR3000 with $G = 60\ \mathrm{mW\,m^{-2}}$ for different present-day shelf depths H_{B}.

S4.3 CH_4 flux assuming that MHSZ is impermeable for methane transport

a) $H_\mathrm{B} = 10$ m

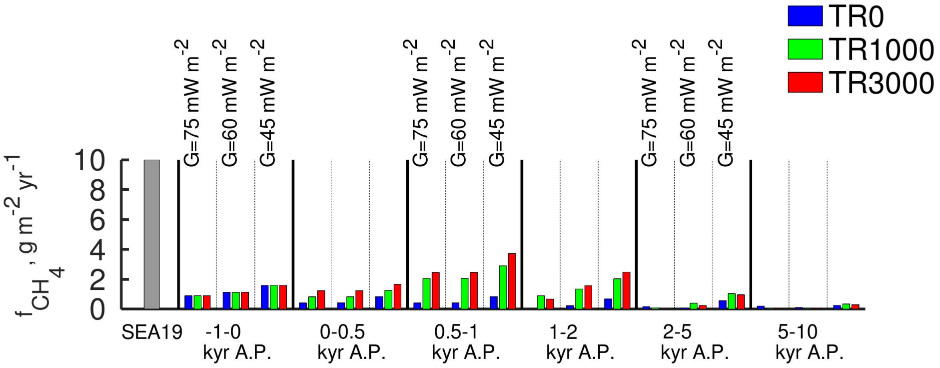

b) $H_\mathrm{B} = 50$ m

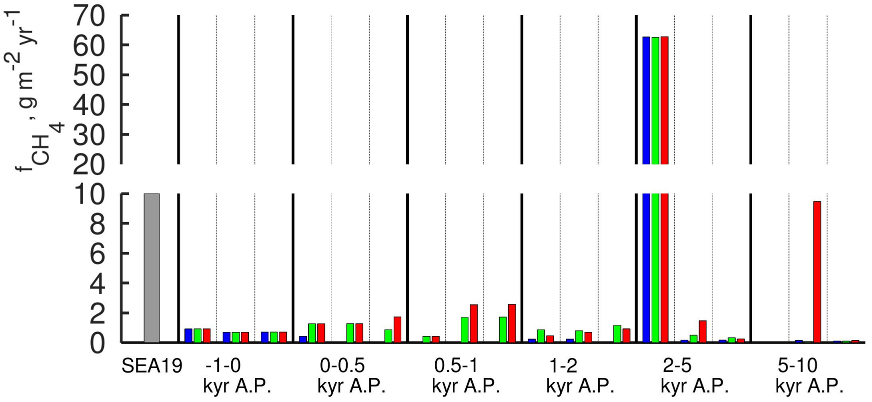

Figure S7: Similar to Fig. 4 of the main text: methane flux from the sediments to the ocean averaged over different time intervals but assuming that MHSZ is impermeable for CH_4 transport.

S4.4 Supplement for pan-Arctic estimates

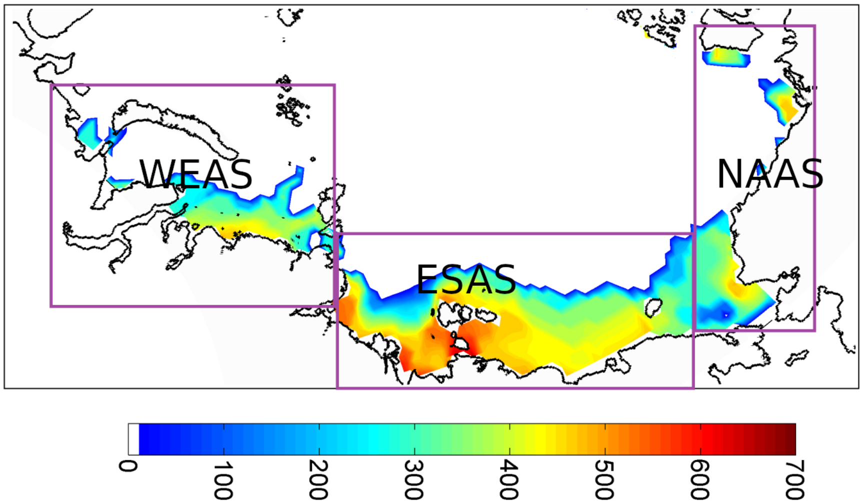

Figure S8: Depth of the subsea permafrost bottom (meters) in 1948 (modified after (Malakhova, 2020)). Rectangles show shelf regions adapted in the present paper: WEAS (West Eurasian Arctic Shelf), ESAS (East Siberian Arctic Shelf), NAAS (North American Arctic Shelf).

Table S4: Permafrost area (10^5 km^2) as simulated by (Malakhova, 2020) at the parts of the contemporary Arctic shelf depicted in Fig. S8 as a function of the present day shelf depth H_B.

H_B, m	WEAS	ESAS	NAAS
≤ 30	1.19	3.16	1.07
from 30 to 75	8.89	4.61	0.74
> 75	0	3.50	0.23

a) $F_{\mathrm{CH_4,w}}$, ESAS

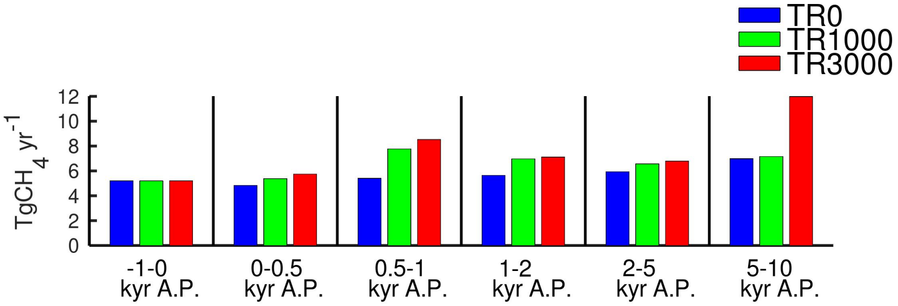

b) $F_{\mathrm{CH_4,w}}$, WEAS

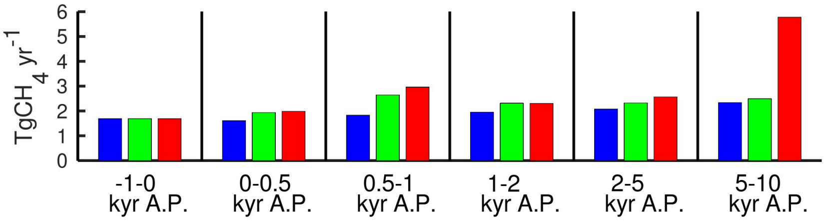

c) $F_{\mathrm{CH_4,w}}$, NAAS

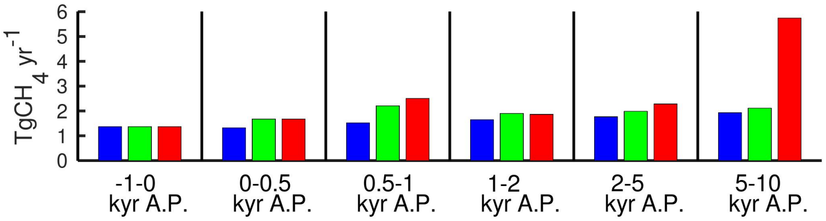

Figure S9: Similar to fig. 6b of the main text but with a breakdown into shelf regions. Please note different ranges of Y-axes for different subplots.

References

Chuvilin E, Bukhanov B, Grebenkin S, et al (2021) Thermal properties of sediments in the East Siberian Arctic seas: A case study in the Buor–Khaya Bay. Mar Petrol Geol 123:104,672. https://doi.org/10.1016/j.marpetgeo.2020.104672

Chuvilin E, Bukhanov B, Yurchenko A, et al (2022) In–situ temperatures and thermal properties of the East Siberian Arctic shelf sediments: Key input for understanding the dynamics of subsea permafrost. Mar Petrol Geol 138:105,550. https://doi.org/10.1016/j.marpetgeo.2022.105550

Galushkin Y, K.A. S, Frolov S (2012) Permafrost formation and degradation in the Urengoy and Kuyumbinskaya areas of Siberia. part 2. influence of variations in thermophysical parameters of frozen rocks on temperature and heat flow distributions with depth. Earth Cryosphere XVI(1):23–29

Ganopolski A, Winkelmann R, Schellnhuber H (2016) Critical insolation-CO_2 relation for diagnosing past and future glacial inception. Nature 529(7585):200–203. https://doi.org/10.1038/nature16494

Malakhova V (2020) The response of the Arctic Ocean gas hydrate associated with subsea permafrost to natural and anthropogenic climate changes. IOP Conf Ser: Earth and Environl Sci 606:012,035. https://doi.org/10.1088/1755-1315/606/1/012035

Malakhova V, Eliseev A (2020) Salt diffusion effect on the submarine permafrost state and distribution as well as on the stability zone of methane hydrates on the Laptev Sea shelf. Ice and Snow 60(4):533–546. https://doi.org/10.31857/S2076673420040058, [in Russian]

Matveeva T, Kaminsky V, Semenova A, et al (2020) Factors affecting the formation and evolution of permafrost and stability zone of gas hydrates: case study of the Laptev Sea. Geosciences 10(12):504. https://doi.org/10.3390/geosciences10120504

Nicolsky D, Romanovsky V, Romanovskii N, et al (2012) Modeling sub–sea permafrost in the East Siberian Arctic Shelf: The Laptev Sea region. J Geophys Res: Earth Surface 117(F3):F03,028. https://doi.org/10.1029/2012JF002358

Petoukhov V, Ganopolski A, Brovkin V, et al (2000) CLIMBER–2: A climate system model of intermediate complexity. Part I: model description and performance for present climate. Clim Dyn 16(1):1–17. https://doi.org/10.1007/PL00007919

Razumov S, Spektor V, Grigoriev M (2014) Model of the post–Cenozoic evolution of the cryolithozone of the shelf of the western part of the Laptev Sea. Oceanology 54(5):637–649. https://doi.org/10.1134/S0001437014040092

Reagan M, Moridis G (2008) Dynamic response of oceanic hydrate deposits to ocean temperature change. J Geophys Res: Oceans 113(C12):C12,023. https://doi.org/10.1029/2008JC004938

Reagan M, Moridis G, Elliott S, et al (2011) Contribution of oceanic gas hydrate dissociation to the formation of Arctic Ocean methane plumes. J Geophys Res: Oceans 116(C9):C09,014. https://doi.org/10.1029/2011JC007189

Sclater J, Christie P (1980) Continental stretching: An explanation of the Post–Mid–Cretaceous subsidence of the central North Sea Basin. J Geophys Res: Solid Earth 85(B7):3711–3739. https://doi.org/10.1029/JB085iB07p03711